Master of Science Thesis
HT2020

Feasibility of single time point dosimetry during 177Lu-PSMA-617 treatments of prostate cancer

Elias Nilsson

Supervisors

Katarina Sjögreen Gleisner, Johan Gustafsson, Erik Larsson and Anna Sundlöv, Lund

Medical Radiation Physics, Lund
Faculty of Science
Lund University
www.msf.lu.se

Abstract

Introduction: Standard dosimetry methods for radionuclide therapies require imaging at multiple time points post injection. An alternative method has been presented in the literature that uses previously acquired pharmacokinetic data to create so-called dose factors. Multiplying the dose factors with an activity concentration (Bq/ml) taken from a single time point measurement results in an estimated absorbed dose (Gy). The dose factors were presented for ^{177}Lu-PSMA-617 therapies for patients with metastatic castrate resistant prostate cancers. Before the new method (1-point method) is applied for clinical use it needs careful validation by comparing it to the standard dosimetry method (2-point method). In this study dosimetry was performed on kidneys, salivary glands and tumors. The resulting absorbed doses were compared between methods to evaluate the applicability of the 1-point method.

Method: Dosimetry was performed on 5 patients, using SPECT/CT images acquired 24 and 96 h post injection. Images were reconstructed with OSEM, using attenuation correction, resolution recovery and model based scatter correction (ESSE). Partial volume correction was performed by convolving the VOI with a Gaussian point spread function and determining the ratio of VOI counts with and without effects of limited spatial resolution. Two dosimetry methods were used, the 2-point method that incorporated images from both imaging time points and the 1-point method. Absorbed doses using the 1-point method were calculated for the two different imaging time points separately. Salivary glands and kidneys were delineated manually, tumor delineation was made using an automated method based on difference of Gaussians. Tumors were categorised into soft tissue and bone lesions based on their mean density and corresponding coefficient of variation, using support vector machines for classification.

Results: Mean absorbed dose (standard deviation) per injected activity to kidneys was 0.56 ± 0.14 (2-point method), 0.59 ± 0.11 (1-point method 24h-image) and 0.44 ± 0.16 (1-point method 96h-image) Gy/GBq, to submandibular glands it was 0.36 ± 0.15 (2-point method), 0.34 ± 0.14 (1-point method 24h-image), 0.23 ± 0.12 (1-point method 96h-image) Gy/GBq, and for parotid glands 0.31 ± 0.15 (2-point method), 0.32 ± 0.13 (1-point method 24h-image) and 0.19 ± 0.14 (1-point method 96h-image) Gy/GBq. Categorisation of tumor type using support vector machines on test data correctly categorised 50 out of 51 tumors.

Conclusion: The 1-point method for performing dosimetry was deemed sufficiently accurate based on the low mean difference in absorbed dose compared to the 2-point method. This applies to images taken 24 h post injection, imaging at 96 hours resulted in poor agreement with the 2-point method.

Förenklad dosimetri i samband med radionuklidterapi

Prostatacancer innebär att det har bildats en elakartad tumör i prostatan. Till en början växer cancern enbart i prostatakörteln. I detta fall har patienten goda möjligheter till att bli botad. Om cancern sprider sig utanför prostatan så minskar möjligheten att bota cancern. Då brukar behandling gå ut på att minska symptom och bromsa spridningen, så kallad palliativ behandling. Radionuklidterapi kan användas som palliativ behandling för prostatacancer. Dessa behandlingar innebär att man tillför ett radioaktivt läkemedel till patienten. Ett radioaktivt läkemedel speciellt anpassat för behandling av spridd prostatacancer är ^{177}Lu-PSMA-617. PSMA-617 är ett läkemedel som ackumuleras i prostata och prostatacancerceller. ^{177}Lu är ett radioaktivt ämne som emitterar så kallade beta-partiklar när den sönderfaller. Dessa beta-partiklar kan orsaka biologisk skada på vävnader. Genom att kemiskt koppla ihop ^{177}Lu med PSMA-617 så skapas ett radioaktivt läkemedel. PSMA-617:s uppgift är att se till att det radioaktiva läkemedlet ackumuleras på prostatacancerceller där ^{177}Lu i sin tur gör biologisk skada på dessa celler.

Absorberad dos är ett mått på hur mycket energi som deponerats per massenhet. Denna storhet går att koppla till den radiobiologiska effekt som orsakas av strålning. Målet med radionuklidbehandlingar är att skada cancerceller, dock så kan även friska vävnader ta skada. Det kan vara fördelaktigt att få en uppfattning av mängden absorberad dos olika friska vävnader har fått under behandlingar. Därför att om man vet mängden absorberad dos ett organ tolererar innan det skadas kan man planera behandlingar utifrån detta. För att beräkna den absorberad dosen till ett organ så krävs det att man vet mängden radioaktivt läkemedel som befinner sig i organet samt hur det utsöndras. Man kan med speciella kameror ta bilder för att se fördelningen av det radioaktiva läkemedlet. Detta kallas single-photon emission computed tomography (SPECT). Dessa bilder är underlag för att beräkna den absorberade dosen. Den nuvarande metoden kräver att man tar flera SPECT bilder, gärna med några dagar mellan bildtagningarna.

En nyligen publicerad artikel beskriver en metod för förenklad dosimetri där det räcker med ett bildtagningstillfälle för att beräkna absorberad dos. Målet med detta arbete var att testa och evaluera den nya metoden. Detta gjordes genom att jämföra absorberade doser beräknade med den nya och den nuvarande metoden. Dosimetri utfördes på spottkörtlar, njurar och tumörer för fem patienter som behandlats med ^{177}Lu-PSMA-617.

Resultatet visade att den nya metoden för att beräkna absorberad dos är genomförbar. Denna slutsats baserades på att det var en liten skillnad i absorberad dos mellan de två metoderna. Detta tyder på att man kan införa den nya metoden utan att påverka de resulterande absorberade doserna på ett markant sätt. Fördelen är att den nya metoden är mindre resurskrävande för klinik och patient.

Contents

1 Abbreviations

VOI - Volume Of Interest

RC - Recovery Coefficient

CT - Computed Tomography

PSMA - Prostate Specific Membrane Antigen

^{177}Lu - Lutetium-177

SPECT - Single Photon Emission Computed Tomography

mCRPC - metastatic Castrate Resistant Prostate Cancer

keV - kilo-electron Volt

SVM - Support Vector Machines

CV - Coefficient of Variation

OSEM - Ordered Subsets Expectation Maximisation

2 Introduction

Dosimetry is used during radionuclide therapies to investigate its relationship to radiation effects on healthy organs and tumors. The resulting absorbed doses can be used for planning future therapy cycles to better individualise treatments. ^{177}Lu-PSMA-617 is a new radiopharmaceutical currently being evaluated in an international phase 3 study for treating metastatic Castrate Resistant Prostate Cancers (mCRPC) [1]. ^{177}Lu-PSMA-617 patients are currently treated with a fixed amount of therapy cycles and administered activity. If dosimetry is implemented in routine use, patients can get a more personalised treatment potentially leading to better treatment results and less side effects. As of now, dosimetry requires multiple images to be acquired with a few days in between each image acquisition, this can be a time consuming process for both patient and personnel. Before dosimetry is implemented for routine use it would be helpful to find a simplified method, as this could relieve the clinic from some of the workload.

Commonly reported adverse events during ^{177}Lu-PSMA-617 treatment are fatigue, nausea and dry mouth [1]. Dry mouth can be linked to damaged salivary glands caused by the treatment, and kidneys have been reported to accumulate PSMA-617 at increased rates compared to other organs [2]. Since these organs potentially are at risk of being damaged during treatment, dosimetry will be performed on these to evaluate the risk of complications. If dosimetry calculations show that the absorbed dose to kidneys or salivary glands exceeds the tolerance absorbed dose. Then dosimetry can be implemented in routine use to plan treatments around these organs, in such a way that a certain absorbed dose is not exceeded.

2.1 Aim

The aim of this study is to perform and evaluate dosimetry using a newly published method for simplified dosimetry [3]. The current way of performing dosimetry involves taking multiple post injection images with a gamma camera while the new simplified version requires only one acquisition. Dosimetry will be performed on five patients given ^{177}Lu-PSMA-617, on tumors and organs-at-risk, using the new and the standard method. The absorbed dose will be compared between the methods to examine the difference. Absorbed dose to risk organs using the standard method will be compared with tolerance absorbed doses to evaluate the risk of toxic effects. By comparing the two dosimetry methods a conclusion will be made whether or not the new

method is sufficiently accurate to be implemented for routine use. Comparing the absorbed doses with tolerance absorbed doses is a way to evaluate for which organs dosimetry is needed.

3 Theory

3.1 Prostate cancer

Prostate cancer is cancer of the prostate gland, often located in the outer parts of the gland. It is the most common type of cancer in Sweden, around 10,000 men are diagnosed every year which accounts for approximately 30% of all cancer cases. It is most common for older men, the median age is 70 years. The biggest risk factor is old age, with some connections to genetics. In the early stages when the cancer is located in the prostate there are usually no or few symptoms and curative treatments are possible with a high chance of survival. Early symptoms are most commonly located in the renal system. The cancer is often slow growing and in some cases treatment is not necessary, instead active monitoring of development is done. Common treatment options for local cancers are external beam radiation therapy, brachytherapy and surgery [4].

In later stages the cancer starts to spread outside the prostate, common locations are lymph nodes and bone. In even later stages it can spread to other organs such as liver and lungs. When the cancer has started to spread curative options are limited. In these cases treatment is often combined with hormonal treatment which intends to reduce testosterone production which most prostate cancers need to continue growth. This usually has initial good results for years. After some time the cancer becomes castrate resistant called castrate-resistant prostate cancers (CRPC) and the cancer can progress without the presence of testosterone. There are many types of palliative treatments and usually a combination of these are used, such as chemotherapy, external beam radiation therapy, radionuclide therapy, and different types of hormonal treatments [5].

^{177}Lu-PSMA-617 is currently used as a second-line therapy after standard treatment has failed. It is injected intravenously and accumulates where PSMA is expressed. For treatment to be effective a high expression of PSMA receptors in cancer cells is needed. This allows for the radiopharmaceutical to accumulate on cancer cells and cause biological damage, thus reducing tumor size, relieving symptoms and preventing tumor growth [6].

3.2 ^{177}Lu-PSMA-617

^{177}Lu-PSMA-617 is a radiopharmaceutical used for treatment of disseminated prostate cancer. ^{177}Lu decays to the stable isotope ^{177}Hf through β^--decay. The β^--particle has a maximum energy of 497 keV with a mean range of 0.23 mm in soft tissue and a half-life of 6.64 days [7]. The combination of a long half-life and β^--emission is desirable in radionuclide therapy. The short range of β^- particles results in high locally deposited energy, this makes it possible to spare nearby healthy tissues while still damaging tumor cells. A half-life of 6.64 days means that ^{177}Lu can cause damage to tumors for multiple days post injection given that it is connected with a pharmaceutical that accumulates on tumor cells. ^{177}Lu also emits γ-radiation including two photon energies useful for imaging with a gamma camera at 113 keV and 208 keV [8]. A simplified decay scheme of ^{177}Lu is shown in figure 1.

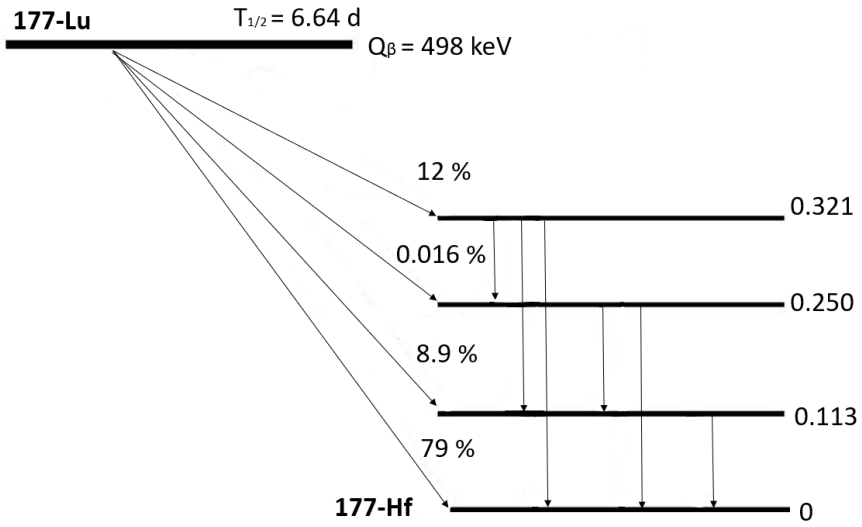

Figure 1: Decay scheme for ^{177}Lu. Decay data taken from [8].

^{177}Lu can be chemically linked to PSMA-617 which is a transmembrane protein that is naturally found on prostate cells and prostate cancer cells. If PSMA is administered intravenously it will accumulate at tissues where PSMA is expressed. ^{177}Lu-PSMA-617 can thus be used as a radiopharmaceutical since PSMA accumulates on cancer cells where ^{177}Lu nuclei will emit β-particles damaging the cancer cells giving a therapeutic effect. Since γ-radiation is also emitted the distribution of the pharmaceutical can be traced using a gamma camera and dosimetry can be performed. Besides

cancer cells, cells in the small intestine, proximal renal tubules and salivary glands also express PSMA [2]. This results in higher uptake of ^{177}Lu-PSMA-617 compared to other healthy organs, potentially causing notable damage. Studies have reported absorbed doses to kidneys at 0.49-0.88 Gy/GBq [9] [10] [11] [12] [13] [14], parotid glands 0.55-1.9 Gy/GBq [9] [10] [11] [12] and submandibular glands 0.5-0.64 Gy/GBq [10] [11].

3.3 Internal dosimetry

The mean absorbed dose $\mathrm{D}(\mathrm{r_T})$ is defined as the mean energy imparted to target tissue $\mathrm{r_T}$ per unit tissue mass [15]. Absorbed dose can be used to calculate risks and treatment effects. The risks can be divided into two categories, the stochastic effects and the deterministic effects. Stochastic effects are related to the risk of developing a radiation-induced cancer which is something that takes years to develop. The deterministic effects depend on the organ or tissue that is exposed and the absorbed dose. Deterministic effects are expected after exceeding a certain absorbed dose. In external beam radiotherapy tolerance absorbed doses have been identified for many organs that indicates the absorbed dose an organ tolerates before permanent damage and loss of function, this can be used for planning treatments. In radionuclide therapy including ^{177}Lu-PSMA-617 treatments there is yet less knowledge about the tolerance doses.

A method for performing internal dosimetry and calculated absorbed dose is described by the The Medical Internal Radiation Dose (MIRD) scheme [16]. The dose rate $\dot{\mathrm{D}}(\mathrm{r_T},\mathrm{t})$ to target tissue $\mathrm{r_T}$ is calculated in the following way

$$\dot{\mathrm{D}}(r_\mathrm{T}, t) = \sum\nolimits_{r_s} A(r_S, t) S(r_T \leftarrow r_S, t), \tag{1}$$

where $A(r_S, t)$ is the time-dependent activity in source tissue r_S and $S(r_T \leftarrow r_S, t)$ is the radionuclide-specific quantity representing the mean absorbed dose rate to target tissue $\mathrm{r_T}$ at time t after administration per unit activity present in source tissue $\mathrm{r_S}$ [16]. When calculating the absorbed dose tabulated S-values are often used, these are based on simulations that are specified for different radionuclides and target anatomies. Equation 1 can be simplified to the following equation assuming the only radiation source is from the target itself and that the target mass is unchanged during irradiation

$$D(r_T, T_D) = \tilde{A}(r_s, T_D) \cdot S(r_T \leftarrow r_S). \tag{2}$$

$\tilde{A}(r_s, T_D)$ is the time-integrated activity. T_D denotes the dose-integration period and is often set to infinity. $\tilde{A}(r_s, T_D)$ equals the total number of

disintegrations in the source tissue and can be calculated as

$$\tilde{A}(r_s, T_D) = \int_0^{T_D} A(r_s, t)\, dt. \tag{3}$$

3.4 Dosimetry using a single posttreatment SPECT/CT

1-point dosimetry is a way of performing internal dosimetry using a single posttreatment scan. The pharmacokinetics has to be known when perform internal dosimetry. The standard method is to take multiple post treatment scans to study the pharmacologic clearance for each patient. 1-point dosimetry uses other methods to estimate the pharmacokinetics. An article by Jackson et al [3] provides a way of performing 1-point dosimetry using previously recorded pharmacokinetics. This was done by normalizing time activity curves for multiple patients to a single measurement time, and using this to estimate a mean and range of time integrated activity values for tumors and different organs. Combining these values with S-factors results in dose factors. Multiplying the dose factors with an activity concentration (Bq/ml) taken from a single time point measurement results in an absorbed dose (Gy). Pharmacokinetics was modeled as a triexponential curve representing an initial uptake phase and two clearance phases. This was done using three SPECT/CT scans taken at 4, 24 and 96 h post injection. The curvefit parameters were used to create a population based reference time-activity curve for tumors and different organs. The resulting time activity curves were multiplied with scaling factors that modify the amplitude of the curve while keeping the relative contribution of the three kinetic parameters. This results in curves that can be normalized for any imaging time point. Tabulated values were presented that can be used to calculate the absorbed dose to several organs and tumors for any post injection time point, using the activity concentration of the organ/tumor derived from one imaging time point. These values are based on a population mean. If a patient deviates from the mean, for example due to some kind of illness, this method might be problematic.

3.5 Single photon emission computed tomography

In order to perform dosimetry during radionuclide therapy the distribution of activity within the patient has to be known. The basic concept of a gamma camera is to detect photons emitted from a radionuclide decay within a patient. These photons will travel to, and be detected by the camera and create an image showing the distribution. The images can be made quantitative

and used for calculating activity concentration. To be able to get quantitative images and improve the resolution of the images there are several components and methods used.

Planar imaging acquires two-dimensional images over a three-dimensional structure. Since images are two-dimensional the activity of overlapping structures is superimposed resulting in an uncertainty when quantifying activity.

SPECT imaging is used to produce three-dimensional images instead thus solving the limitation presented by planar imaging. In SPECT imaging the camera is not static, instead the camera head rotates around the patient acquiring data from multiple angles. These images are later reconstructed into tomographic images where each voxel value represents an activity concentration. This presupposes that corrections for attenuation and scatter is included and also adjusted for sensitivity. SPECT imaging takes several minutes, during this time it is important that the patient remains still. Motion during measurement results in motion artefacts. This leads to blurry images and misrepresentation of organ/tumor position. SPECT imaging is often combined with CT imaging (SPECT/CT) primarily for attenuation correction. The CT image provides anatomical information that can be used for obtaining mass of organs. CT images also provide much better anatomical positional information than the SPECT, which can be useful for localizing where in the patient the radiopharmaceutical uptake is.

The collimator is the first part of the camera reached by the photons. It is used to identify lines of response where the radioactive decay has occurred. Parallel hole collimators consist of multiple small holes separated by lead septas. Photons that are not incident perpendicular relative to the collimator are attenuated in the septa. Photons incident perpendicular relative to the collimator have a chance to pass through the holes and reach the scintillation crystal. The design of the collimator affects the resolution and sensitivity of the camera. Sensitivity of the camera is a way to quantify the number of detected photons relative to the amount of decays from the source. The sensitivity is increased if the holes are larger, have thinner septa, and a shorter length. The trade-off with increasing the sensitivity is that resolution worsens. The resolution of the camera is a measure of its ability to depict objects accurately. Spatial resolution is defined as the cameras ability to distinguish between two point sources as separate objects. The resolution of the camera is better with smaller holes and longer septa [17].

After the photons have passed the collimator they reach the detector, often composed by a NaI(Tl) crystal. Scintillation materials emit light when interacting with ionizing radiation and are made of materials with crystal structures. These have a conduction band and a valence band. When charged particles enter the scintillator they excite the crystal structure, it will then quickly deexcite and send out a photon in the process. The energy of these photons can be altered by doping the crystal. Doping the crystal allows energy levels within the bandgap. Since the energy of these emitted photons is lower than the crystal band gap, the crystal is transparent to its own light meaning the emitted photons will not cause further excitation [18].

The scintillator is connected to an array of photomultiplier tubes. The first part is the photo cathode, when a photon hits the cathode it transfers its energy to the cathode and a photo electron is emitted. The next part consists of dynodes placed in series. The photo electron is accelerated towards the dynodes due to an applied high voltage. Every time the electron hits a dynode more electrons are knocked out. The amount of electrons created increase with number of dynondes and the applied voltage. Lastly the electrons are collected by the anode and the current is measured, which is proportional to the energy of the incoming radiation. This process has converted the incoming light from the crystal into an electric pulse that is readable. By using an array of photomultiplier tubes the point of interaction can be determined [19].

3.5.1 Attenuation and scatter

There are several factors that affect activity quantification and quality before photons reach the camera. One of the more notable is photon attenuation. This is the process of photons not reaching the camera due to attenuation in the patient caused by photoelectric absorption or Compton scattering. The degree of attenuation depends on the length the photon's travel through the patient and the composition of the matter. Not correcting for photon attenuation result in artefacts and a large underestimation of activity.

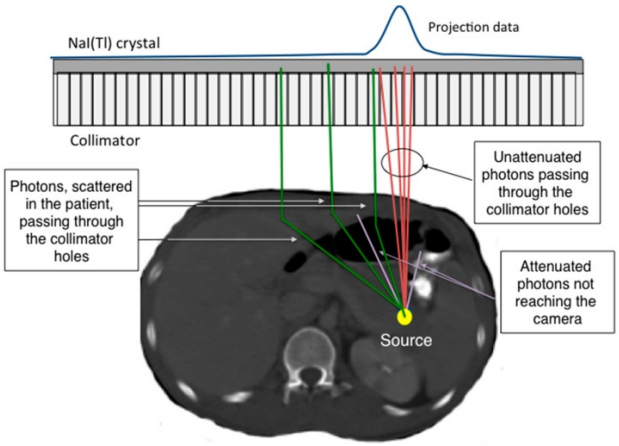

Figure 2: Photon attenuation and scatter, image from [20].

Photon interaction with atoms can result in Compton scattering. In the process photons lose energy and change direction. Photons that scatter and pass through the collimator have a misrepresentation of the origin of the photon. The detector assumes that the photon originates from the position where the photon scattered and not the original source. This causes reduction of contrast and a false increase of counts. The impact of this effect can be reduced by using an energy window. The energy window removes counts that are not within a certain energy interval, thus removing counts from photons that have scattered and lost some of its energy. Another important part of the energy window is to select a specific photon energy to detect. This can be used when determining source activity if the probability of detecting the specific decay is known [20].

3.5.2 SPECT reconstruction

Acquired projection from SPECT are reconstructed to convert them into tomographic images. The basics of iterative reconstruction methods is that they start with an initial guess of the image, then compute projections from that image. Calculated and measured projection data are compared, the image is then updated based on the calculated difference between the projections. The difference is a type of error image and is used to improve the initial guess. This process can be done iteratively, each time improving the reconstruction. Depending on the algorithm too many iterations can reduce the signal to noise ratio as well as being time-consuming. Corrections for

photon attenuation and photon scatter can be included in the reconstruction, using the morphological information based on the CT image in its calculation [20].

The images reconstructed used in this study were reconstructed using ordered-subsets expectation-maximisation (OSEM) which is a variation of the ML-EM method. The advantage of the OSEM algorithm is that reconstruction is faster making it more practical for clinical use. Scatter correction was done using effective source scatter estimate (ESSE) [21] which is a model based scatter-compensation method incorporated into the reconstruction.

3.6 Partial volume correction

The partial volume effect is the loss of apparent activity in a volume of interest (VOI) when an object partially inhabit the sensitive volume of the camera, described by the point-spread function (PSF) of the system. In the case of SPECT images the PSF describes the effect of the limited resolution of the gamma camera. The sensitive volume is the volume from which emitted photons can be detected by the camera without being attenuated in the collimator [22]. This leads to a decrease in accuracy and an underestimation of activity when quantifying activity in a VOI, due to counts ending up outside of the VOI. Partial volume correction is used to reduce the impact of this effect and therefore increase the accuracy of activity measurements. The Recovery Coefficient (RC) is an estimation of the fraction of counts that are reduced in a VOI due to spill-out

$$RC = \frac{\text{measured activity in object VOI}}{\text{true activity in object}}. \tag{4}$$

Calculating the fraction of the measured activity in object VOI and the true activity in the object results in a recovery coefficient. The RC grows closer to unity for larger volumes and more spherical shapes since the effect of spill out diminishes. Increasingly smaller and more uneven shapes tend to lower values.

3.7 Support vector machines

Support vector machines (SVM) are learning algorithms that can be used in machine learning for multiple purposes, one of them being classification of data points called support vector classification (SVC). A SVC algorithm separates categorised data by finding the optimal hyperplane that separates

the data points into the given categories. A hyperplane is a subspace with dimension one less than that of its ambient space. SVC can be further used to predict in what category new non categorised data points belongs in, this is done by calculating the data position relative to that of the hyperplane. Support vectors are the data points located closest to the hyperplane, these data points define the position and orientation of the optimal hyperplane. The distance between the hyperplane and the closest data-points is called the margin. The goal of the SVM algorithm is to find the hyperplane that produces the largest margin between hyperplane and support vectors (maximising the margin).

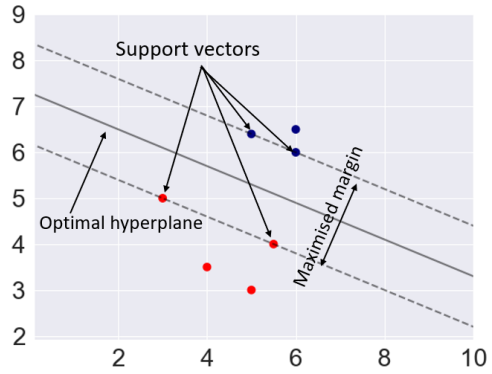

Figure 3: Figure showing hyperplane, support vectors and margin.

If data points cannot be perfectly separated by a hyperplane, a soft margin can be used. The soft margin allows for some data points to be misclassified or within the margin, these data points can not be support vectors. The soft margin is also a way to avoid overfitting the data. SVM with soft margins calculate the optimal solution by trying to, maximise the margin and minimizing the amount of misclassified data points. This is an optimization problem as the two goals often conflict with each other and there is no perfect solution. The trade-off between maximizing the margin and avoiding misclassification is controlled by a parameter denoted C. The value of C quantifies how large the penalty should be for misclassifying data-points. By choosing a low value of C a low penalty for misclassification is given. This causes the algorithm to look for a larger margin hyperplane at the cost of misclassifying some data points. Increasing the value of C increases the penalty, resulting in a smaller margin hyperplane if that hyperplane reduces the amount of misclassified data. If the data is not linearly separable by a hyperplane the so called ”kernel trick” can be implemented which is a

method that uses a linear classifier to solve a non linear problem. The kernel function maps the data points onto a higher dimensional space where there is a linearly separable solution [23] [24].

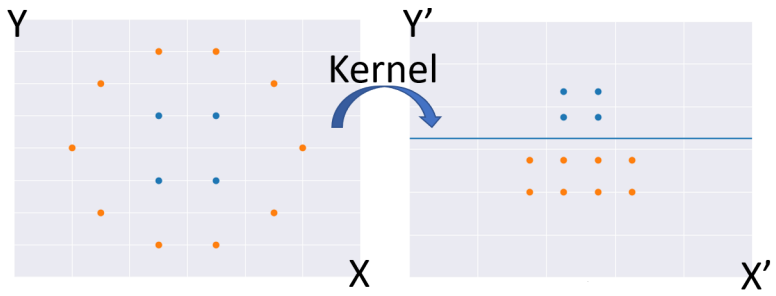

Figure 4: A simplified sketch showing how non linearly separable data in dimension d can become linearly separable after being projected onto a higher dimensional space >d.

4 Method

4.1 Patient data

Patients included in this work were treated as part of a phase 3 trial called VISION [1], which studied the safety and effectiveness of ^{177}Lu-PSMA-617 treatments. In VISION, patients were randomized in a 2:1 ratio for ^{177}Lu-PSMA-617 treatment (7.4 GBq every 6 weeks for four to six cycles) plus protocol-permitted standard care or standard care alone, standard care alone representing the control group. Included patients have PSMA-positive mCRPT which is defined as one or more PSMA-positive metastatic lesions and no PSMA-negative lesions. PSMA-positive status was determined using ^{68}Ga-PSMA-11 PET–CT imaging, if uptake of ^{68}Ga-PSMA-11 was greater than that of liver parenchyma in one or more metastatic lesions of any size in any organ system it was classified as PSMA-positive. Patients with PSMA-negative metastatic lesions were excluded. Selection was further based on 19 inclusion criteria and 11 exclusion criteria (NCT03511664, clinicaltrials.gov). Some of the inclusion criteria were: a life expectancy over 6 months, progressive mCRPC and adequate organ function [1].

Five metastatic castration-resistant prostate cancer patients treated with ^{177}Lu-PSMA-617 at Skåne University Hospital were included in our study. After each therapy cycle posttreatment imaging was done using SPECT/CT

to study the pharmacokinetics of ^{177}Lu-PSMA-617. There were 1 or 2 images taken per therapy cycle, the first taken at around 24 h post injection and the second at around 96 h post injection. The number of cycles ranged between 4 and 6 resulting in a total of 43 SPECT/CT images for all patients. One patient only underwent the first posttreatment SPECT/CT for all therapy cycles and could therefore not be included in the majority of this study.

4.2 Imaging parameters

SPECT/CT-images were acquired with a GE Discovery NM/CT 670 (GE HealthCare, Haifa, Israel) using a medium energy general purpose collimator with a 15 % energy window centered at 208 keV. Image acquisition was performed with the following parameters: 60 projections, 30 seconds per projection, 128 x 128 matrices with pixel size 4.42 x 4.42 mm^2 and 3 bed positions covering 115 cm from head to thighs. Images were reconstructed using OSEM with 8 iterations and 6 angles per subsets, using attenuation correction, resolution recovery and the model based scatter correction method ESSE [21]. Calibration was done through measurement of sensitivity in air. The resulting SPECT images are constructed of activity per voxel and the CT images in Hounsfield unit.

4.3 Delineation of tumors, kidneys and salivary glands

Segmentation of kidneys was done manually. Each kidney was outlined in the transverse plane for every slice where the kidneys were visible, using the CT images for guidance. The resulting VOIs were stored in the form of a binary masks with value one inside the VOI and the value 0 outside. This was done for every patient, therapy cycle and imaging time point.

Segmentation of tumors was done using the SPECT images as basis. The segmentation process was done using an automated segmentation method based on difference of Gaussians [25]. The image is filtered with Gaussian filters of different widths, subtracting these filtered images from each other results in a high-pass filtered image. On the high pass filtered image a region growing algorithm is applied. The seeds are automatically placed from image coordinates based on a predefined threshold and determining the centroid of each pre-segmented region. The automated segmentation method cannot differentiate tumors from non-malignant uptake of ^{177}Lu-PSMA-617 such as intestinal contents, bladder, kidneys and salivary glands. The images were therefore reviewed afterwards and false positive VOIs were detected and

deleted manually. False positives were identified based on location, shape and appearance in both CT and SPECT image. It was important to differentiate between intestinal content/intestine and lymph node lesions as these are located in the same region and can have similar shape. This was done by looking at the excretion rate (by comparing imaging time point one and two) as lymph nodes retain PSMA for a long period compared to intestine and intestinal content disappear between imaging time points. Kidneys and salivary glands were removed in this process to be manually delineated later. An example of how false positives appear can be seen in figure 5.

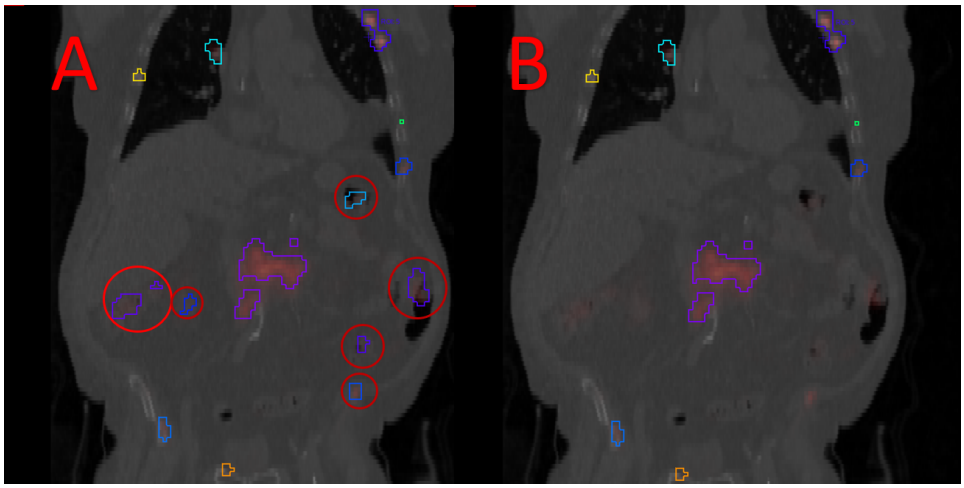

Figure 5: Before (A) false positives were removed and after (B). False positives highlighted in red.

The first attempt at delining salivary glands was done using the CT-images for guidance. This turned out to be problematic for two reasons. Low contrast between salivary glands and surrounding structures made accurate delining difficult and patient movement between the CT-image and SPECT-image lead to a mismatch between the images. The resulting VOIs had a large reduction of activity concentration caused by the patient movement, due to the salivary gland position in the CT-image not corresponding to the salivary gland position in the SPECT-image. To avoid activity underestimation, segmentation was done manually using the SPECT-image as guidance instead. Resulting VOI included most of the counts originating from the salivary glands, however the VOI did not represent correct CT data. The CT-images are used in the dosimetry calculation to extract the density which is then later used to calculate the mass. Since these VOI would

sometimes include air or bone instead of salivary glands a fixed density of the salivary glands was used at 1.03 g/cm^3 [26]. Due to the excretion rate of ^{177}Lu-PSMA-617 in salivary glands being rather fast, the visible part of the salivary glands in SPECT-images is reduced the further imaging occurs from the injection time. To counteract the reduction of apparent salivary gland volume in SPECT-image, the VOI was delined in the first imaging time point first, and then copied over to the second imaging time point, thus having the same volume of the salivary glands between imaging time points. For the second imaging time point the VOI was moved to correlate with the position of the salivary glands. Minor adjustments were done to make sure as little as possible of the activity was left out. An example of a mismatch between SPECT and CT is shown in figure 6, the VOI was created based on the SPECT image were the shape of the parotid glad is evident (A). The same VOI placed in the CT image does not appear over the parotid glands, instead it appears over the bone structure of the skull.

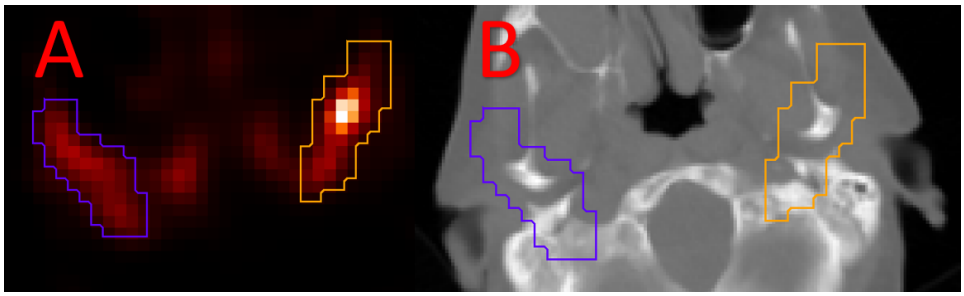

Figure 6: VOI delined guided by the SPECT image (A), the same VOI in the CT-image (B).

4.4 Partial volume correction

To compensate for partial volume effects, recovery coefficients were calculated for each VOI using equation 4. RC was calculated by convolving the binary masks with a 10 mm Gaussian point spread function and determining the ratio of VOI counts with versus without effects of limited spatial resolution. The convolution with a Gaussian was done to simulate the impact of limited spatial resolution of the gamma camera with an assumed resolution of 10 mm. The RC were then used when calculating activity concentration to correct for the partial volume effect.

When plotting the RC for tumors as a function of volume it showed a strong dependence on volume but also on shape for a given volume. Around half of the tumors had a RC below 0.5. The RC has a large impact on the absorbed dose calculation and large corrections can potentially affect the uncertainty. Therefore a cutoff RC was needed, tumors that have a RC lower than the limit should not be included as the uncertainty was deemed too large. To better understand the distribution of RC and to evaluate if the method works as intended, further calculations were done to investigate the dependence on volume and shape. This was also used for deciding the cutoff.

The first attempt to better understand the RC was to create a bubble chart that showed the relationship between tumor volume, RC and a quantity that represents the shape of the VOI. This quantity, called ”shape”, was set to be the area of a VOI divided with the volume of the VOI. Since $\frac{A}{V} \propto \frac{3}{r}$ "shape" was defined as $\frac{A}{V^{2/3}}$. This gives "shape" a range of values, spherical shapes have lower values and more oblong shapes have increasingly higher values. The area was calculated by applying an erosion operation on a VOI and subtracting this from the original VOI. This results in a VOI with only the outermost voxels remaining. Shape was calculated by dividing the volume of the VOI with only the outermost voxels (the area) with the volume of the original VOI. RC was then plotted as a function of shape with the volume as the size of the data points.

A second study was made to better understand the relationship between RC, shape and volume. This consisted of constructing voxelised spheres with the same volume as tumor VOIs and calculating a RC for spheres and tumor VOIs. Since a sphere is the shape that results in the highest RC a comparison between sphere and tumor VOI give an indication of how much RC depends on the shape of the tumor VOIs. A plot was made showing a side by side comparison between RC for sphere and tumor VOI as a function of volume.

4.5 Single time point dosimetry

The VOIs created during segmentation represent the tumor/organ location and are binary masks containing ones and zeros with value one inside the VOI and zero outside. Multiplying these masks with the SPECT/CT images result in a matrix containing values within the VOI in units of MBq/voxel for SPECT and Hounsfield units for CT. Mean activity concentration (AC)

within a VOI was calculated as the total value of that matrix divided with the volume (V), volume was calculated as the number of voxels within a VOI multiplied with voxel volume. The resulting activity concentration was divided with the RC to compensate for partial volume effects. Activity concentration was calculated using the following equation

$$AC = \frac{\sum(SPECT \cdot M)}{V \cdot RC}, \tag{5}$$

where M is the mask corresponding to the particular VOI. The tabulated dose factors (Ω) that were used to convert activity concentration into absorbed dose [3] used an estimated density for all tumors and organs of 1 g/ml. In order to get more accurate results, the true densities were of interest. These were calculated using conversion values based on phantom measurements with an CIRS Model 062 Electron Density Phantom (Norfolk, VA, USA). Figure 7 shows the Hounsfield unit to density conversion for CT images taken with a tube voltage of 120 kV.

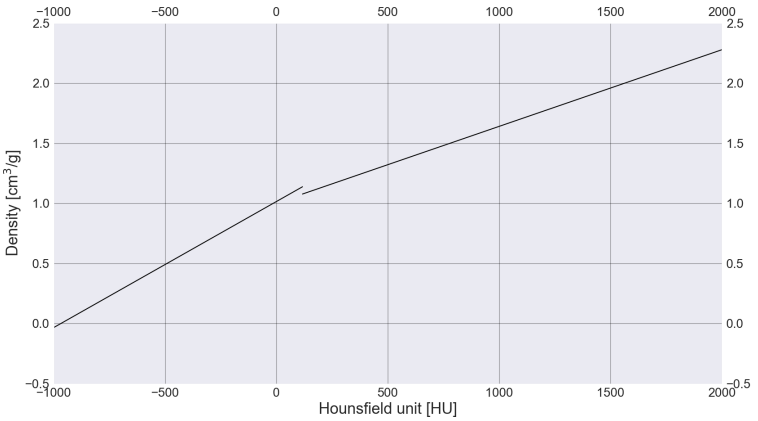

Figure 7: Density as a function of Hounsfield unit.

For every VOI the average density within the VOI was used. The absorbed dose (D) was then calculated as

$$D = \frac{AC \cdot \Omega}{Density}. \tag{6}$$

Ω is the tabulated dose factor presented by Jackson et al [3]. Tumor activity concentration was originally calculated using the VOI volume from the corresponding imaging time point. It turned out that the VOI volume decreased more between imaging time points than first expected. Since there is only circa 3 days in between the images the tumor volume is not expected to decrease in a noticeable way. Therefore absorbed dose calculations were also performed using the average volume of tumor VOIs from image 1 and 2 to see if there was a noticeable difference.

4.6 Dosimetry using two imaging time points

4.6.1 Obtaining the S-value

S-values used for dosimetry were obtained using IDAC DOSE sphere module [26]. The input parameters into IDAC DOSE sphere module are radionuclide and organ material. The S-values are based on spheres. The output parameters are S-values in the unit mGy/MBq·h dependant on sphere volume. The resulting values are given for a few specific volumes. To get a curve for which any volume has a corresponding S-value, a curve fit was done using the following equation

$$\mathcal{S} = A \cdot m^{-B}, \tag{7}$$

where A and B are curve fit parameters. To get more accurately chosen S-values the S-values were changed to be dependent on mass instead of volume. This was done by multiplying the volume with the density of the given organ.

It is also possible to get S-values from IDAC DOSE that incorporates the shape of the kidneys. With this method one S-value is given for a kidney mass of 422 g, representing both kidneys. To evaluate how well the interpolation works and the impact of using spheres instead of kidney shape. A comparison was done between S-value from IDAC DOSE that incorporates the shape of the kidneys, compared to S-value from IDAC DOSE sphere module were S-values are interpolated from a number of sphere volumes. The comparison was done by calculating the fraction,

$$\frac{S_{Kidney} \cdot 422}{S_{Sphere} \cdot 211} = 1.006. \tag{8}$$

The difference was calculated to be 0.6%, thus the chosen method using IDAC spheres and interpolation to different volumes was deemed sufficiently accurate to use for further calculations.

4.6.2 Obtaining $\tilde{A}$

The absorbed dose D was to be calculated using equation 2. For this $\tilde{A}$ had to be calculated first. This was done by evaluating the following integral

$$\tilde{A} = \int_0^\infty A_0 \cdot e^{-\lambda t}\, dt \; = \frac{A_0}{\lambda}. \tag{9}$$

In order to solve for $\tilde{A}$, A_0 and λ had to be determined. To obtain these values the following equation system was solved,

$$\begin{cases} A_1 = A_0 \cdot e^{-\lambda t_1} \\ A_2 = A_0 \cdot e^{-\lambda t_2} \end{cases} \tag{10}$$

t is the imaging time point and A is the activity at time point t, subscript 1 and 2 denotes imaging time point 1 and 2. A_1 and A_2 was calculated by multiplying the activity concentration with the volume of the organ/tumor of interest. By combining the two previous equation λ could be calculated,

$$\lambda = \frac{\ln \frac{A_1}{A_2}}{t_2 - t_1}, \tag{11}$$

with λ being known A_0 could be determined as

$$A_0 = A_1 \cdot e^{\lambda t_1}. \tag{12}$$

$\tilde{A}$ could then simply be calculated by inserting A_0 and λ into equation 7.

$$\tilde{A} = \frac{A_0}{\lambda}.$$

With S and $\tilde{A}$ being known the absorbed dose was calculated using equation 2.

4.7 Tumor classification

A method to distinguish soft tissue lesions from bone lesions was desired. The hypothesis was that the two tumor types could be separated based on mean density within a VOI under the assumption that bone lesions have a higher density. The first step was to look at CT-images for a few treatments and for each VOI determine if it was a bone or soft tissue lesion. A plot was made showing the different tumor types as a function of density. From the graph a distinct separation could be seen at around 1.1 g/cm^3, however

there were also several outliers and this method for separating tumor types was deemed unsatisfactory.

A new attempt was done, this time calculating the coefficient of variation (CV) for density within the VOI. The hypothesis was that bone lesions have a higher CV within a VOI due to the high density of bone compared to the lower density of malignancies and surrounding tissue, while a soft tissue lesion has a uniform density within the VOI. A plot was made showing the CV within a VOI as a function of mean density. This showed a clear separation without any outliers.

The next step was to automate the process of classifying tumor type. This was done using machine learning with support vector machines. The program was trained using the previous data points that had been classified as bone or soft tissue. Training data was collected for varying imaging time point and therapy cycle. At least one image was used from each patient to include a wide range of data. The penalty term was modified in a way to create a broad margin between tumor types to avoid overfitting the data. In the training data two data points were within this margin. These data points shape the separation line controlled by the penalty term C. For every tumor VOI the standard deviation divided with mean density was calculated and used as an input parameter. The program used these values to predicted tumor type. Tumor dosimetry was then divided into bone and soft tissue lesions.

More data points were manually categorised to validate the program. These data points were used as test-data to examine how many of them that would have been correctly categorised if the program had been applied to them, indicating the accuracy of the method.

5 Results

5.1 Partial volume correction

Figure 8 shows the tumor RC as a function of volume. It can be observed that the RC increase with increasing volume until the curve flattens around 0.7. Shape dependent dispersion of RC can be observed for a given volume.

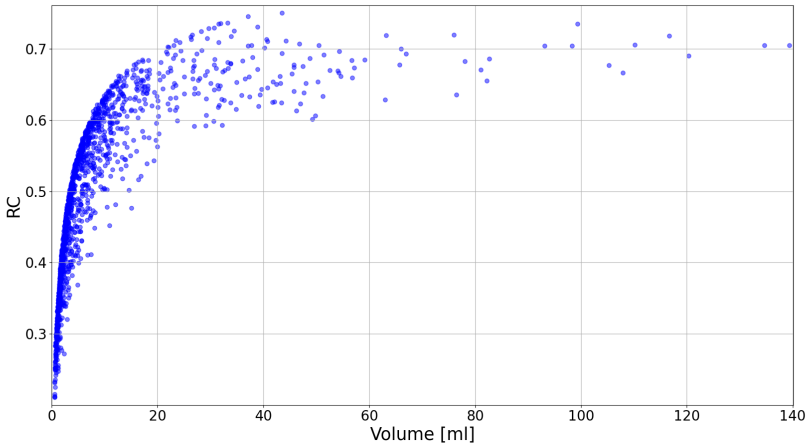

Figure 8: Calculated RC for tumors as a function of volume.

Figure 9 shows the RC for kidneys. Since kidneys are rather similar in volume and shape the RC do not fluctuate as much as for tumors with most kidneys having a value between 0.8 and 0.85. The RC is also larger than for the tumors.

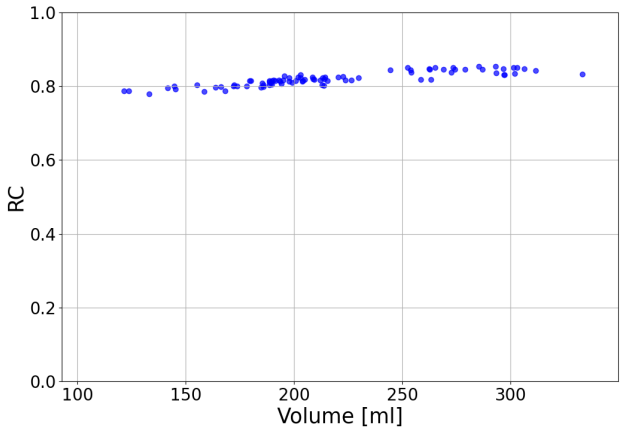

Figure 9: Calculated RC for kidneys as a function of volume.

Parotid glands had RC between 0.72-0.79 and submandibular glands 0.62-0.72. RC as a function of volume behaved similar as for kidneys with slightly increasing RC as volume increase and a small dispersion of RC close in volume.

RC for tumors as a function of shape can be seen in figure 10. With increasing value of "shape", RC also increases. The goal was to get a better understanding of the RC dependence on shape of tumor VOI separated from its dependence on volume. The problem with this graph is that there is still a strong dependence on volume. It shows that smaller volume VOIs tend to be rounder.

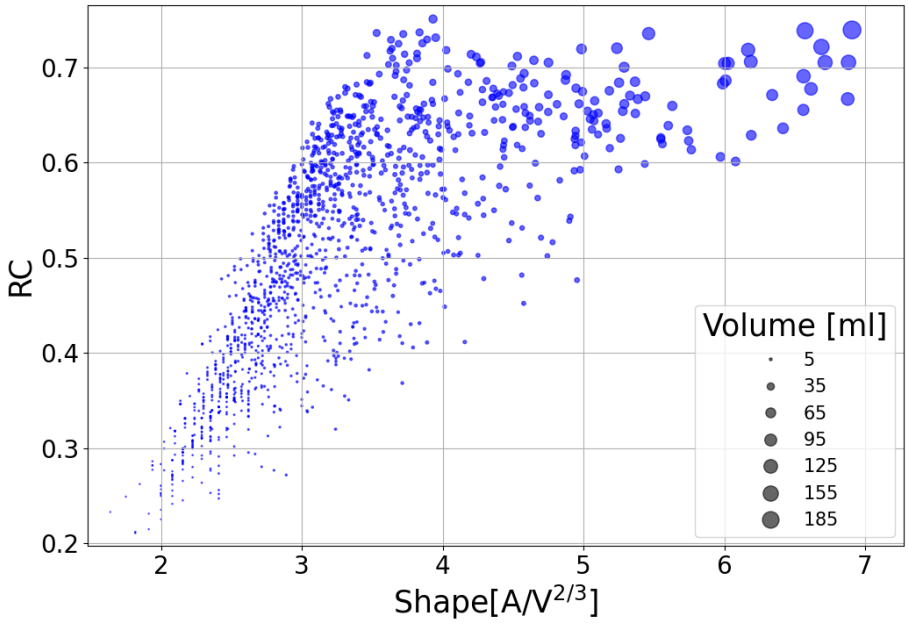

Figure 10: RC as a function of "shape". Spherical shapes have lower values and more oblong shapes have increasingly higher values

The second attempt at better understanding RC dependence on shape is shown in figure 11. Here RC have been calculated for spheres with the same volume as tumors and plotted alongside RC for tumors. The dependence on shape seems to play a larger roll for smaller volumes, at 10 ml there is a difference of more than 30% between the lowest RC for tumors and sphere. This difference appears to decrease for larger volumes. A cutoff was decided at RC = 0.5. The values that were removed are primarily tumors with small volumes. For volumes above 10 ml almost all tumors are included and there is no dependence on shape if they are above or below the cutoff. However, there is an area around the cutoff limit below 10 ml were only the more

spherical shapes are included. The smallest volume still included is as small as 3.3 ml. Before the cutoff there were a total of 1506 tumor VOI, after the cutoff at 0.5 there were 759 left (50%).

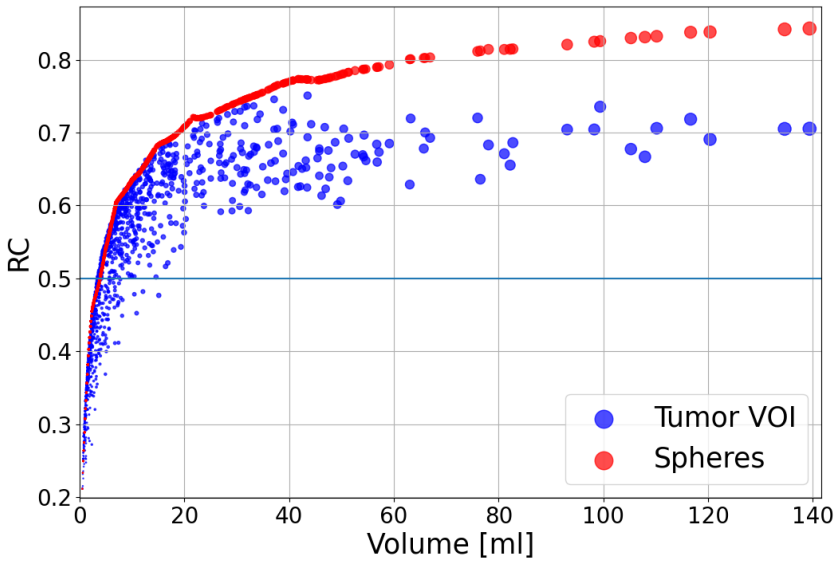

Figure 11: RC values for tumor VOI and spheres as a function of volume.

5.2 Tumor classification

A plot over the data points used for training the tumor identification program is presented in figure 12. The two dotted lines show the margin and the solid line is the hyperplane separating the data. There appears to be large fluctuation in density and standard deviation for bone lesions while soft tissue lesions are more homogeneous, as hypothesised. Data points marked in green is the data that the SVM used for calculating the hyperplane. Outside the margin are the support vectors. Inside the margin are the points used in the penalty term.

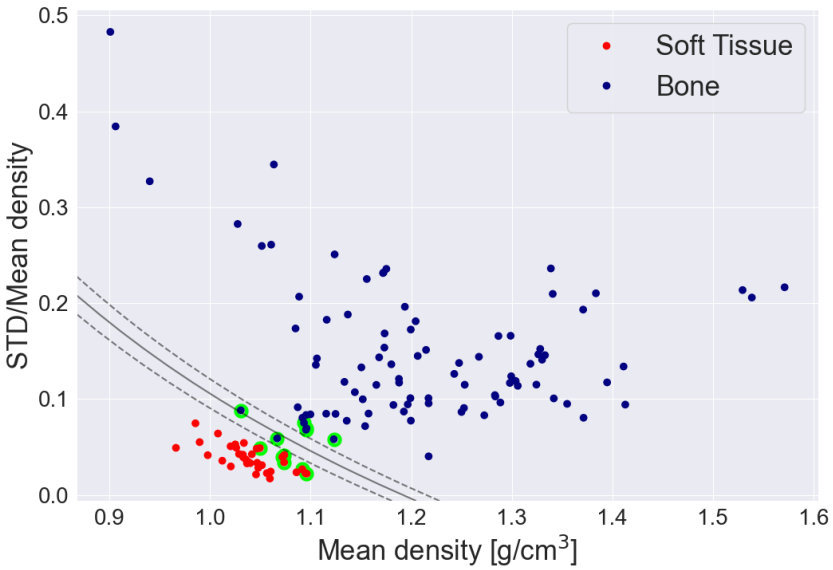

Figure 12: Visual representation of how tumor type is identified and categorised for training data points.

To validate the tumor classification program categorised data points were presented with the separation line in figure 13. 98% of tumors were correctly categorised.

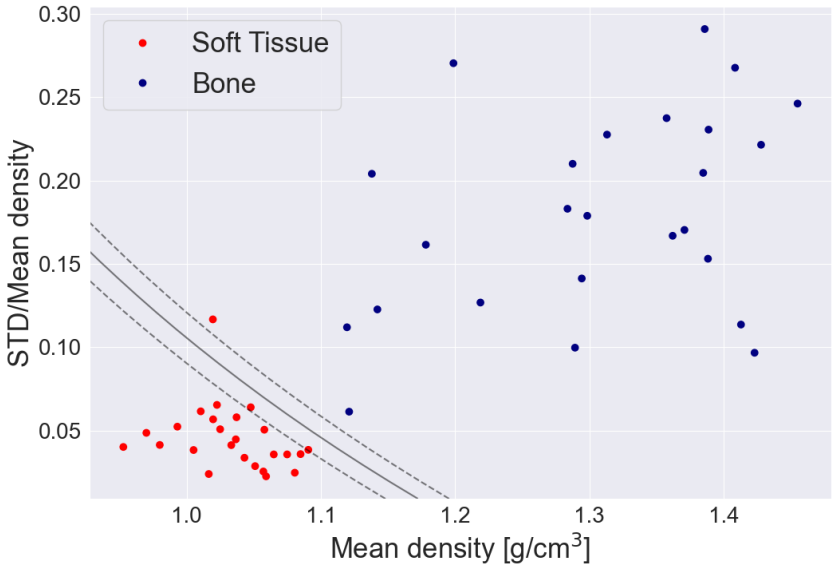

Figure 13: Categorised data points plotted with the hyperplane that separates the data points into the given categories. 50 out of 51 tumors are correctly categorised.

The tumors above the RC cutoff are shown in figure 14 with the separation line, data points ending up under the hyperplane are classified as soft tissue lesions, data points above are classified as bone lesions. It appears to show the same distribution as the training data. The cluster for soft tissue lesions is distinct around density 1 g/cm^3 below 0.1 STD/Mean density and the same spread can be seen for bone lesions as the training data. Relative to the amount of data few data points are within the margin (3%).

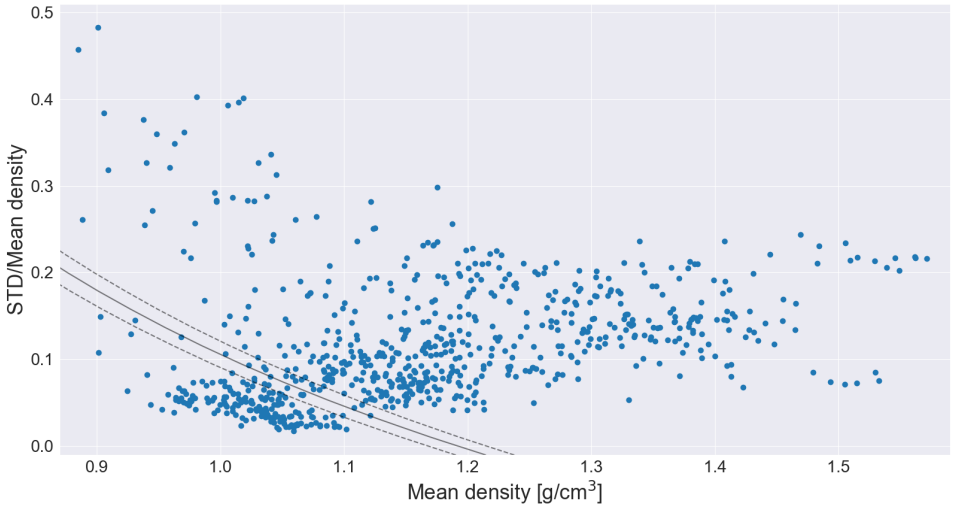

Figure 14: Separation of tumor type for all data points.

5.3 Dosimetry

Kidney absorbed dose per injected activity is presented in figure 15 for the different dosimetry methods. Overall the absorbed dose derived from the 2-point method seems to correspond better with the absorbed dose derived from the 1-point method using the first imaging time point taken at around 24 h (orange bar) compared to the second imaging time point at around 96 h (green bar). Patient 1, 2 and 4 show agreement between the 2-point method and the one point method for the first image, however for patient 3 there seems to be a large difference between the methods. There does not seem to be a correlation between therapy cycle and absorbed dose.

Figure 15: Absorbed dose to kidneys using the different dosimetry methods. Therapy cycle presented in parentheses on the x-axis.

Cumulative absorbed dose over all cycles and absorbed dose per therapy cycle is shown in table 1. The 1-point method using image 1 shows agreement with the 2-point method for patient 1, 2 and 4. For these patients there is only a 0.9, 3.2 and 6.6 % difference in cumulative absorbed dose to kidneys between the two methods. 1-point method using image 2 results in a lower absorbed dose compared to the 2-point method for all patients, and the 1-point methods does not seem to work well for patient 3 with 41% higher and 39% lower absorbed dose.

Table 1: Absorbed doses to kidneys using different dosimetry methods. In parentheses the percentage difference is presented. Calculated as the difference between given method and 2-point method, divided with 2-point method.

Dosimetry method	Patient 1	Patient 2	Patient 3	Patient 4
2-point, cumulative absorbed dose [Gy]	24.42	13.25	13.24	23.72
2-point, absorbed dose/therapy [Gy]	4.07	4.42	3.31	5.93
1-point image 1, cumulative absorbed dose [Gy]	24.64 (+0.90%)	13.67 (+3.2%)	18.62 (+41%)	22.15 (-6.6%)
1-point image 1, absorbed dose/therapy [Gy]	4.11	4.55	4.65	5.54
1-point image 2, cumulative absorbed dose [Gy]	18.51 (-24%)	11.01 (-17%)	7.89 (-39%)	20.38 (-14%)
1-point image 2, absorbed dose/therapy [Gy]	3.09	3.70	1.97	5.10

The Bland Altman plots presented in figure 16 show the agreement between the 2-point method and 1-point method image 1 (A) and image 2 (B). Difference is calculated as 1-point method minus 2-point method in unit of Gy/GBq. Imaging time point 1 has a low mean difference between the two methods with a mean difference of only 0.03 Gy/GBq. Imaging time point 2 seems to systematically yield a lower absorbed dose.

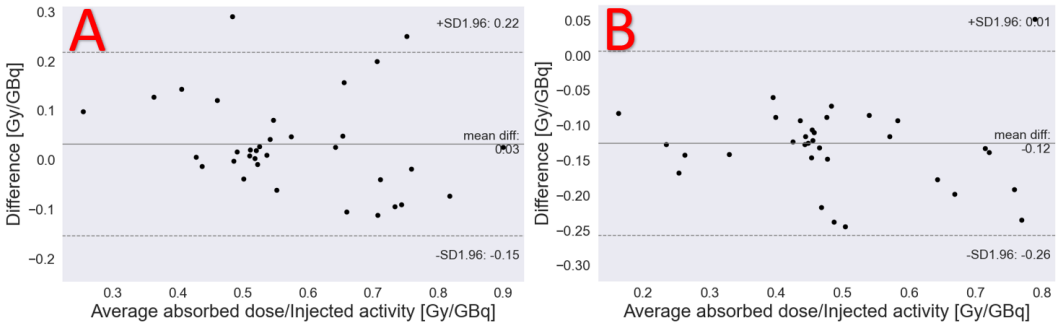

Figure 16: Bland Altman plots comparing 2-point method with 1-point method imaging time point 1 (A) and imaging time point 2 (B) for kidneys.

For salivary glands the first imaging time point corresponds more with the 2-point method compared to the second, seen in figures 17 and 18. There is no obvious change in absorbed dose between therapy cycles. Due to salivary glands sometime not being within the field of view there are fewer therapy cycles included than for kidneys and tumors.

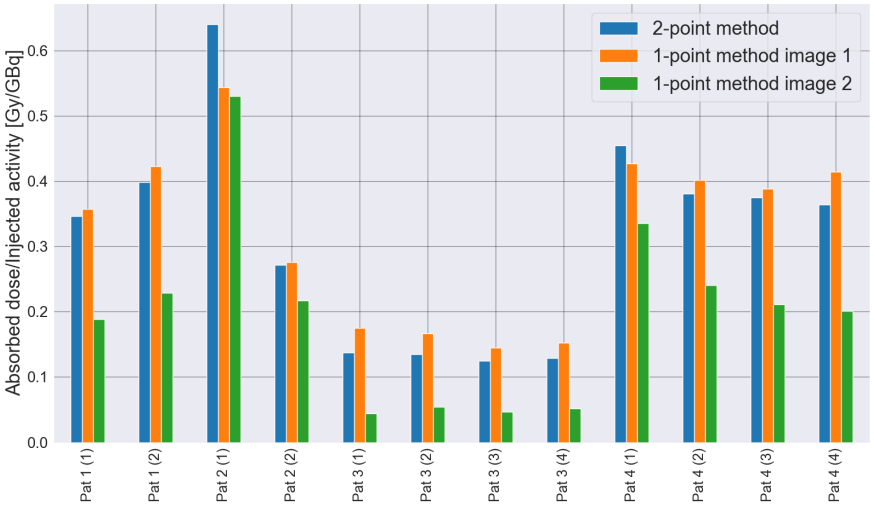

Figure 17: Absorbed dose/injected activity for parotid glands.

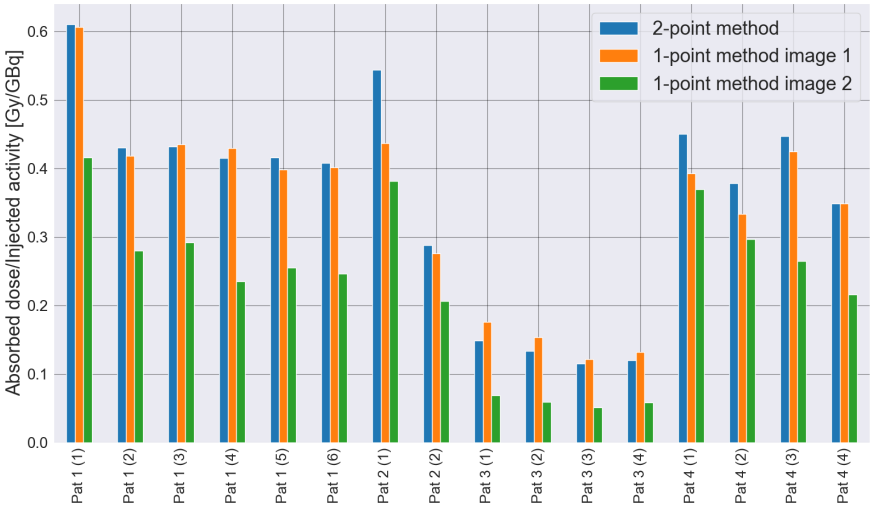

Figure 18: Absorbed dose/injected activity for submandibular glands.

In table 2 cumulative absorbed dose over all cycles is shown (where the salivary glands are within the field of view).

Table 2: Absorbed dose to salivary glands using different dosimetry methods. P stands for parotid glands and S for submandibular glands. In parentheses the percentage difference is presented. Calculated as the difference between given method and 2-point method, divided with 2-point method.

Dosimetry method	Patient 1	Patient 2	Patient 3	Patient 4
2-point, cumulative absorbed dose [Gy] P	6.05	6.94	4.05	11.77
1-point image 1, cumulative absorbed dose [Gy] P	6.33 (+4.6%)	6.44 (-7.2%)	4.97 (+23%)	12.45 (+5.8%)
1-point image 2, cumulative absorbed dose [Gy] P	3.38 (-54%)	5.88 (-15%)	1.53 (-62%)	7.52 (-36%)
2-point, cumulative absorbed dose [Gy] S	22.31	6.36	4.06	12.05
1-point image 1, cumulative absorbed dose [Gy] S	21.61 (-3.1%)	5.60 (-12%)	4.52 (+12%)	11.45 (-2.7%)
1-point image 2, cumulative absorbed dose [Gy] S	13.87 (-38%)	4.62 (-27%)	1.84 (-55%)	8.74 (-27%)

Bland Altman plots for salivary glands presented in figure 18 show that the first imaging time point results in the best agreement with the 2-point method with a mean difference of only +0.01 (parotid glands) and -0.01 (submandibular glands) Gy/GBq. The second imaging time point has systematically underestimated the absorbed dose resulting in a negative mean difference.

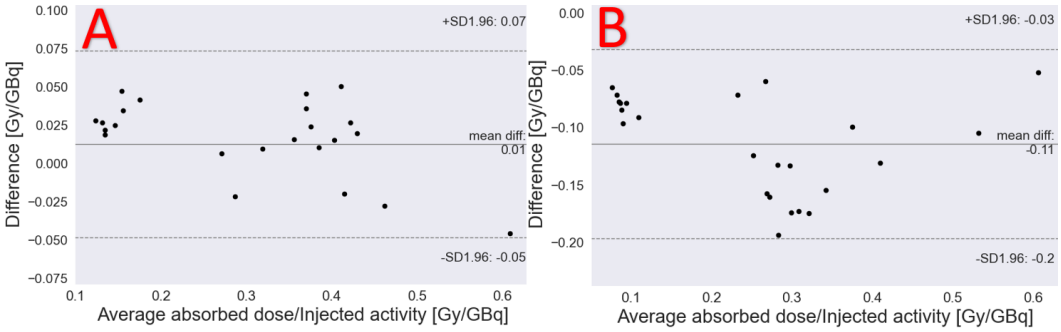

Figure 19: Bland Altman plots comparing 2-point method with 1-point method imaging time point 1 (A) and imaging time point 2 (B) for parotid glands.

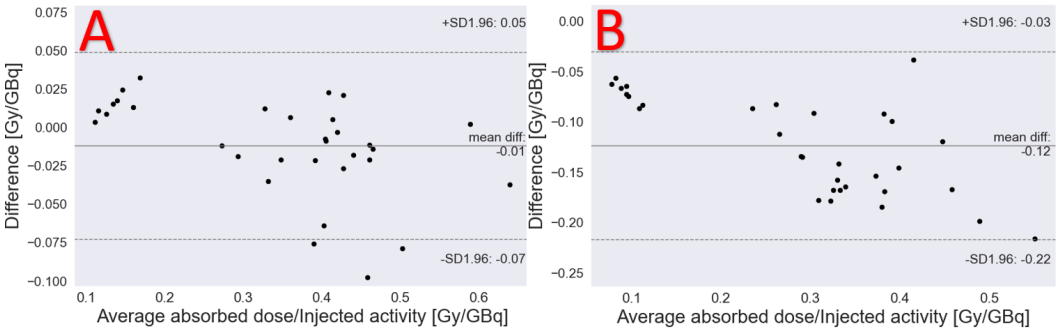

Figure 20: Bland Altman plots comparing 2-point method with 1-point method imaging time point 1 (A) and imaging time point 2 (B) for submandibular glands.

The boxplot in figure 21 shows absorbed dose/injected activity to bone lesions. Number of tumors is presented in parentheses above the boxes and therapy cycle is presented in parentheses on the x-axis. It seems that the absorbed dose and number of tumors decrease with each therapy cycle with a few exceptions and that the 2-point method correlates best with the second imaging time point. It appears as patient 2 and 4 have a wider range and generally larger absorbed dose to tumors compared to patient 1 and 3. For the 1-point method the absorbed dose calculation were done using tumor VOIs from respective imaging time point.

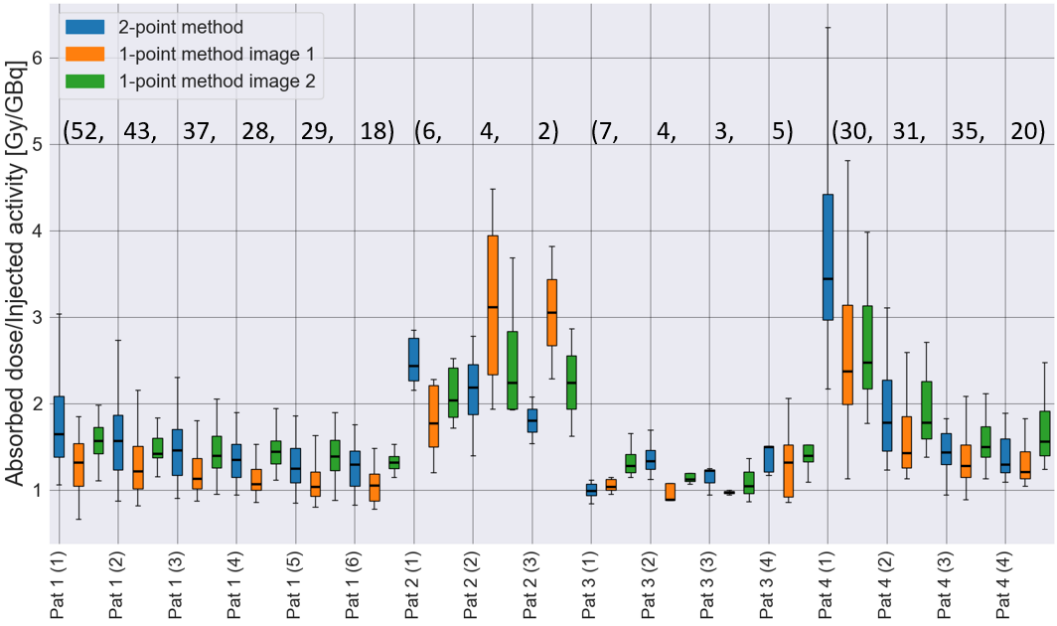

Figure 21: Absorbed doses to bone lesions, volume derived from respective image time point. Number in the top equals the number of tumours included in the analysis.

In figure 22 absorbed dose to soft tissue lesions are presented. Patient 1 had only bone lesions and is therefore not shown in this boxplot. The same trend of decreasing absorbed dose per cycle can be observed, it is however uncertain at what imaging time point the 1-point method correlates the best with the 2-point method.

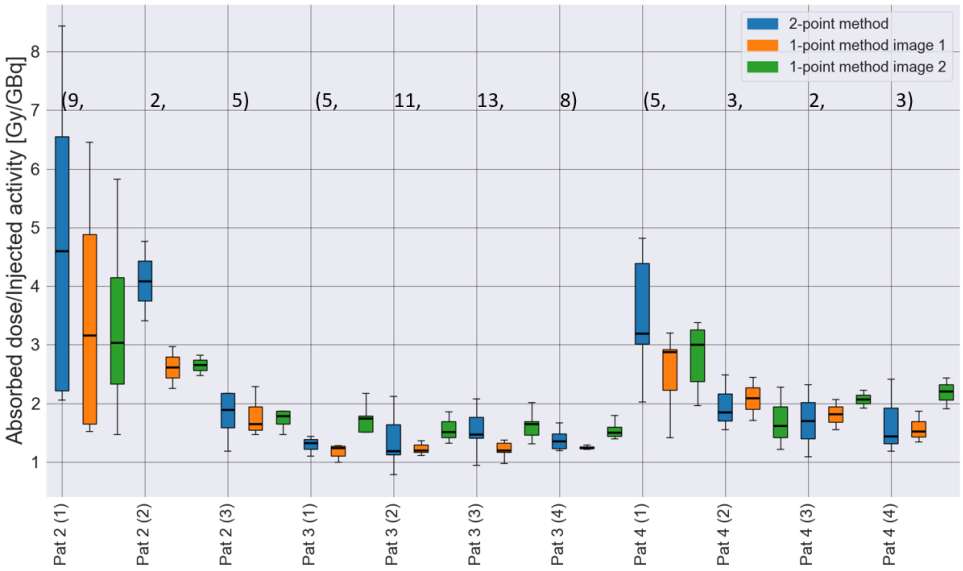

Figure 22: Absorbed doses to soft tissue lesions, volume derived from respective image time point. Number in the top equals the number of tumours included in the analysis.

Since the volume difference in tumor VOI between imaging time points turned out to be larger than expected, the same absorbed dose calculation were done using the average volume between imaging time points, presented in figures 23 and 24. This resulted in the absorbed dose to increase for imaging time point 1 and decease for imaging time point 2. The absorbed dose calculations are the same for the 2-point method which already uses both imaging time points and average volume.

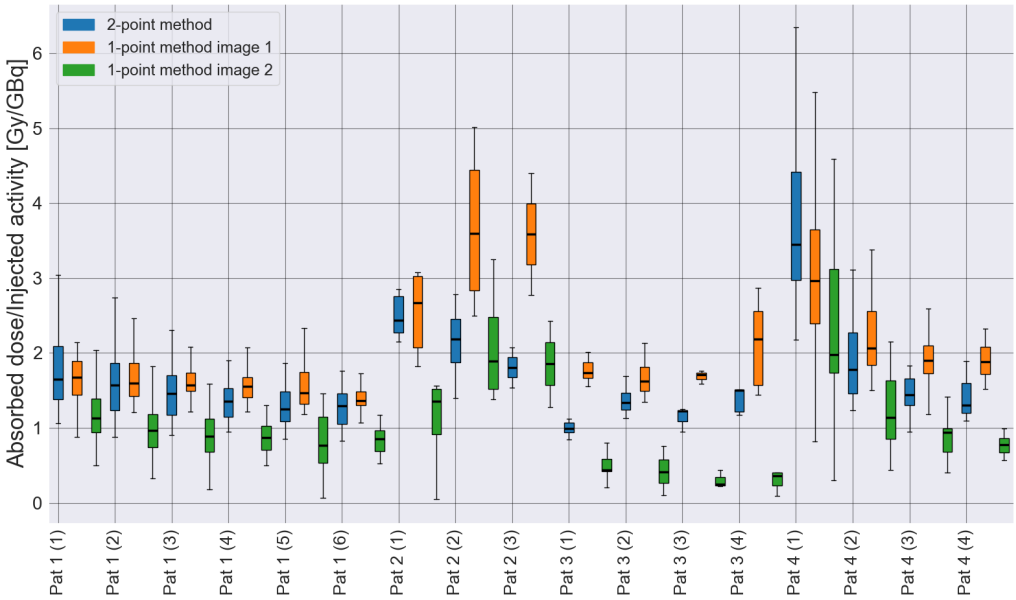

Figure 23: Absorbed doses to bone lesions, volume calculated as the average from the two image time point.

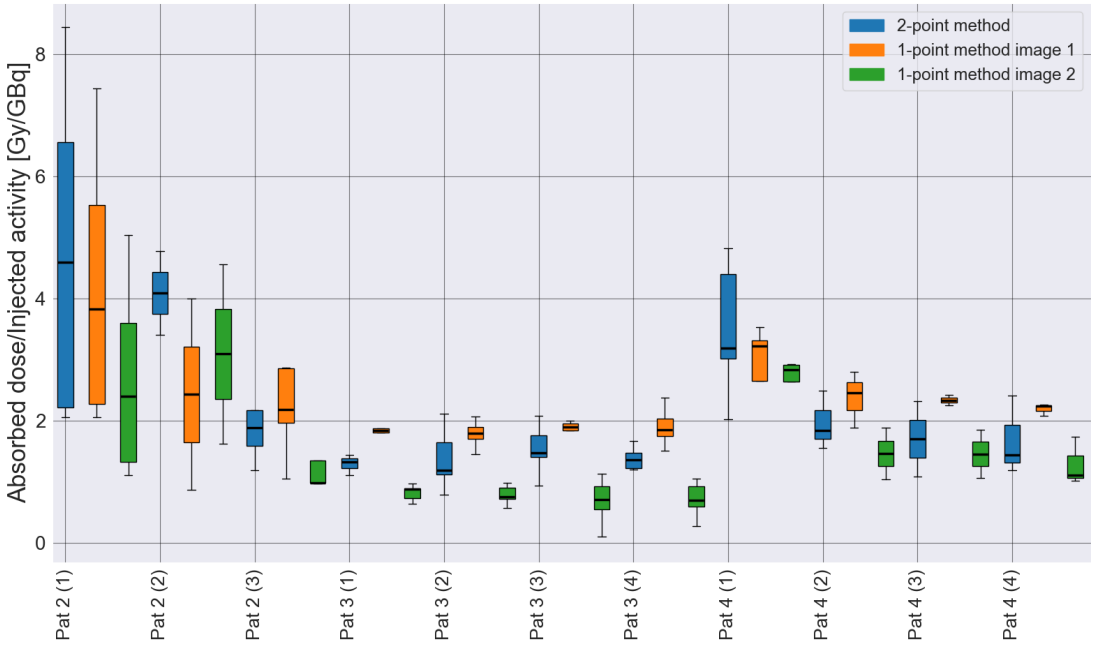

Figure 24: Absorbed doses to soft tissue lesions, volume calculated as the average from the two image time point.

Since calculation based on average volume produced the best agreement between 2-point method and 1 point method, Bland Altman plots are presented for those calculations, figure 25 and 26. Calculations based on volume taken from corresponding imaging time point had lower mean difference for the second imaging time point, -0.15 for bone and -0.20 Gy/GBq for soft tissue, but a larger difference for the first imaging time point, -0.37 for bone and -0.44 Gy/GBq for soft tissue.

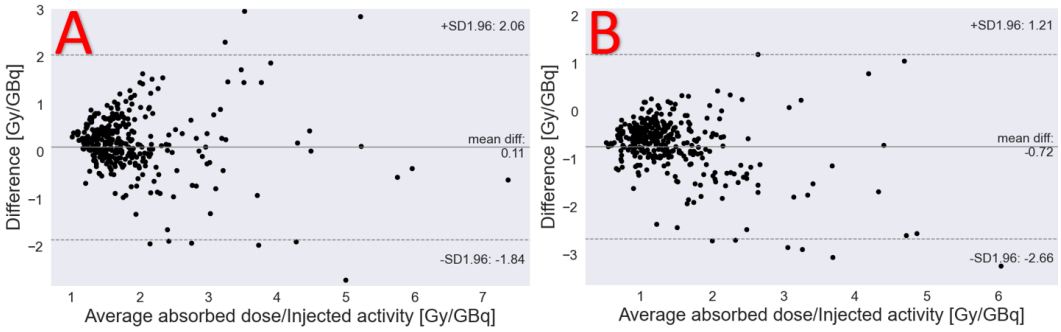

Figure 25: Bland Altman plots comparing 2-point method with 1-point method imaging time point 1 (A) and imaging time point 2 (B) for bone lesions.

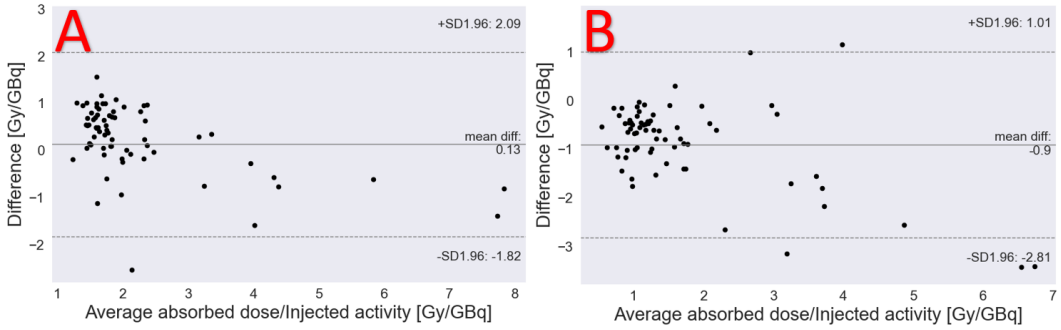

Figure 26: Bland Altman plots comparing 2-point method with 1-point method imaging time point 1 (A) and imaging time point 2 (B) for soft tissue lesions.

5.4 Effective half-life

In table 3 effective half-life is presented for different organs and tumors. Patient 3 has the lowest effective half life for all organs and tumors. This

correlates with the absorbed dose calculation were this patient also has the lowest absorbed dose to the different tissues.

Table 3: Effective half-life ($T_{1/2,eff}$) of ^{177}Lu-PSMA-617 for organs and tumors. Presented as the mean half-life for the different therapy cycles with corresponding standard deviation.

	Patient 1	Patient 2	Patient 3	Patient 4
$T_{1/2,eff}$ in kidneys [h]	35.9 ± 2.14	43.9 ± 5.14	29.6 ± 2.02	43.1 ± 13.2
$T_{1/2,eff}$ in submandibular glands [h]	33.3 ± 1.70	40.0 ± 3.63	26.7 ± 0.65	39.1 ± 6.94
$T_{1/2,eff}$ in parotid glands [h]	28.9 ± 0.94	42.3 ± 7.40	22.5 ± 1.47	31.9 ± 3.97
$T_{1/2,eff}$ in bone lesions [h]	62.4 ± 17.4	51.1 ± 15.9	28.4 ± 9.20	51.4 ± 15.1
$T_{1/2,eff}$ in soft tissue lesions [h]	NO DATA	55.6 ± 11.4	44.1 ± 16.3	71.1 ± 18.9

6 Discussion

6.1 RC

How much the RC affects the uncertainty of the absorbed dose can be difficult to estimate. If the model for partial volume correction was perfect any RC could be used without effecting the uncertainty of the absorbed dose calculations. The more realistic scenario is that the method is not perfect and that larger corrections entail larger uncertainties. For kidneys and salivary glands the RC were relatively large. RC is still likely the largest factor for uncertainty when determining activity concentration but to a lesser extent than that of tumors. Calculated RC for tumors ranges all the way from 0.2-0.75, this brought difficulties. Removing the tumors with low RC from the absorbed dose calculations would reduce the uncertainty. The problem is that a large part of the data would be removed in the process. Calculations based on "shape" and spheres were done to better understand the RC and help decide on how large to make the cutoff. The cutoff was decided at 0.5 which removed half of the tumor data. At 0.5 there is still a correction of 50% in total activity within the VOI. Such large corrections are likely to affect the uncertainty in a negative way. Further increasing the cutoff was decided against as it would remove too much data. Those graphs also confirmed that the RC depends on shape, as it should, and can fluctuate for over 30% within a given volume.

When removing tumors with a RC below 0.5, smaller volume tumors are also removed, excluding tumors with a volume below 3.3 ml from absorbed

dose calculation. These smaller volume tumors have larger uncertainties in absorbed dose compared to larger tumor volumes mainly due to small changes in VOI size results in a relatively larger change in activity concentration. Boxplots made from the tumors with RC below 0.5, show that if smaller tumors had been included the range of tumor absorbed dose would increase but the median absorbed dose would not be affected in a major way. The reason behind a larger range of absorbed dose is likely due to the uncertainty in determining volume. A small tumor can also have a very high mean activity concentration resulting in a very high absorbed dose, larger tumors are more likely to have some colder areas over its volume and declining activity concentration towards edges of the VOI making the mean activity concentration lower.

6.2 Tumor classification using machine learning

To separate soft tissue lesions from bone lesions the tumor classification program was created. The program was validated by testing it on categorised data points. This resulted in 98% of tumors being correctly classified, indicating that the overall accuracy of the program is 98%. When applying the method to the tumor data shown in figure 14 it is observed that the data points seem to follow the same distribution as the training data. There is however a region around mean density 0.92 and STD/Mean density 0.15 were there are a few data points in the actual data but not in the training data. This means that the model was created without considering data points in that area. It is possible that with more training data in that region that the separation line would change slightly. 3% of the data was within the margin, these are the data points with the largest uncertainty of classification. Considering only 3% were within the margin, and those data points are still more likely to be correctly classified than not, this method worked well without effecting the tumor dosimetry results in a major way. If it is desired to remove some of the potentially false identifications, data within the margin could be removed. This would likely remove most of the incorrect identification at the cost of a few percent of the data.

6.3 Dosimetry and comparison of dosimetry methods

For dosimetry purposes it would have been advantageous to acquire more images and at later time points. This would have increased the accuracy of the 2-point method thus making the comparison between methods and with tolerance absorbed doses more reliable. A head fixation would reduce motion

artefacts. This would improve the accuracy of the activity concentration and make delineation of salivary glands easier and more accurate. A diagnostic quality CT could potentially improve the contrast and make delineation of tumors and salivary glands based on the CT-images possible. This would improve the accuracy when quantifying volumes of salivary glands and tumors.

In this study, only 4 out of 5 patients had data that was sufficient for dosimetry evaluations. These patients had different tumor burden, tumor location and different previous treatments. It is also possible they had different illnesses that affected the pharmacokinetics. This might cause absorbed doses to organs and tumors to differ substantially between patients. Considering the small sample size of patients the mean absorbed doses would potentially differ with a larger patient group.

Absorbed dose to kidneys and salivary glands has been reported to correlate with body weight and total tumor burden [27]. This did not appear to be the reason behind the difference is absorbed dose between patients in this rapport, as no correlation between absorbed dose to kidneys/salivary gland and tumor burden/body weight was observed.

6.3.1 Kidneys

High contrast between kidneys and surrounding tissues in CT-images made manual delineation based on the CT-images possible. Due to this, kidney volumes are likely more accurately determined than for salivary glands and tumors. Other articles have presented slightly higher absorbed doses than those in this study 0.88 ± 0.4 [9], 0.6 ± 0.36 [10], 0.72 ± 0.21 [11], 0.82 ± 0.25 [12], 0.49 ± 0.17 [13] and 0.6 [14] Gy/GBq compared to 0.56 ± 0.14 (2-point method), 0.59 ± 0.11 (1-point method image 1) and 0.44 ± 0.16 (1-point method image 2) Gy/GBq average for the 4 patients. For most of them the resulting absorbed doses from the 2-point method and the 1-point method image 1 are within the standard deviation from the other articles. It is difficult to say if there is something that has lead to a systematic underestimation of the absorbed dose or not. One article even presented lower absorbed doses compared to the 2-point method. However since only 4 patients were included in this study and the highest absorbed dose is more than double that of the lowest, it is possible that the average absorbed dose would change if more patients were included.

Three out of four patients showed good agreement between the 2-point method and the 1-point method using image time point 1. However patient 3 was an exception with poor agreement between methods. A possible cause of this is that the patient suffered from some kind of kidney malfunction. This patient's left kidney was twice the size of an average kidney, and his right was half that of a normal kidney. The half-life of ^{177}Lu-PSMA-617 in kidneys for this patient was only 29.6 h compared to the average for all patients of 37.5 h. The 2-point method compute individualized pharmacokinetics. This entails that the method is not particularly sensitive for irregularities in kidney function as it includes the individual shape of the time-activity curve. The same does not apply for the 1-point method that uses average pharmacokinetics for a large amount on patients. This makes the method inaccurate for patients that does not have normal kidney function. Therefore the 2-point method should be applied to patients with known kidney problems/diseases for accurate absorbed dose calculations. The Bland Altman plots in figure 16 shows that the superior imaging time point is the first one around 24 h with a mean difference of only 0.03 Gy/GBq. Time point 2 could potentially be used if the conversion factors are adjusted to increase the absorbed dose since the underestimation seems to be systematic.

6.3.2 Salivary glands

The biggest problem during salivary gland dosimetry was during segmentation. Low contrast and patient movement created problems that were difficult to solve without affecting the uncertainty of the absorbed dose calculations. The chosen method has its limitations, the main one being that dosimetry is performed on the parts of the salivary glands that are shown in the SPECT image, which does not necessarily correspond to the actual anatomy of the salivary gland. The mismatch of SPECT and CT image also affects the attenuation and scatter corrections. The average parotid gland mass for an adult male is 20-30g [28]. The average parotid gland mass derived from the VOIs in this study is 50 g, indicating a large overestimation of mass leading to an underestimation of absorbed dose. The average being so high was largely due to patient 3 with an average mass of 80 g, possibly explaining why his absorbed dose was lower than for the others. It is possible that the patient has an abnormally large parotid gland. The more likely scenario is that the gland appears larger due to motion artefact and poor resolution of the image. Average submandibular mass is 10-15 g [28] compared to the average of 20 g in this study. If salivary gland dosimetry is to be done in the future, there are some improvements that can be done to make dosimetry

easier and reduce the uncertainty. Some sort of head fixation should be used. This will reduce motion artefacts and lead to a better match of SPECT and CT image and reduce the amount of counts that are misplaced. Current CT images were of low quality acquired primarily for attenuation correction. Diagnostic quality CT images would potentially improve the contrast. With these improvements manual segmentation could be performed using the CT images for guidance, resulting in a more accurate volume calculations which results in more accurate absorbed dose calculations.

Absorbed dose to parotid glands is lower than what other articles have presented, 1.17 ± 0.31 [9], 0.56 ± 0.25 [10], 0.55 ± 0.14 [11] and 1.9 ± 1.19 [12] Gy/GBq compared to 0.31 ± 0.15 (2-point method), 0.32 ± 0.13 (1-point method image 1) 0.19 ± 0.14 (1-point method image 2) Gy/GBq average for the 4 patients. Note that patient 3 reduced the average absorbed dose noticeably and was the only patient with an absorbed dose below the average. Other articles presented a wide range of mean absorbed doses 0.55 - 1.9 Gy/GBq with large standard deviations. A wide range in absorbed dose was also presented in this rapport, the highest absorbed dose to parotid glands is circa 5 time larger than the lowest. This might be due to the difficulties during dosimetry or that the absorbed dose differs a lot between therapy cycles and patients. Considering the segmentation method and the motion artefacts this method presented large uncertainties. A possible reason behind the low absorbed dose is a combination of an overestimation of salivary gland mass and an underestimation of activity. From the SPECT images it was evident that many counts had spread out over the image, the magnitude of this on the absorbed dose is hard to estimate but has most likely affected the results is a noticeable way.

Absorbed dose to submandibular glands present lower absorbed doses compared to other articles similarly as for parotid glands, most likely due to the same reasons 0.5 ± 0.15 [10] and 0.64 ± 0.4 [11] Gy/GBq compared to 0.36 ± 0.15 (2-point method), 0.34 ± 0.14 (1-point method image 1) and 0.23 ± 0.12 (1-point method image 2) Gy/GBq average for the 4 patients.

6.3.3 Tumors

Tumor dosimetry presented several difficulties that affected the uncertainty of the dosimetry calculations. Many of these problems were hard to deal with due to the large amount of tumors. This meant that manual solutions were time consuming and not suitable in the long run or for clinical use. There-

fore automated solution were used for segmentation and tumor classification.

The biggest problem that arose during tumor dosimetry was how to accurately decide tumor volume. For future tumor dosimetry a better method of deciding tumor volume has to be found as with the current way there is potentially a large difference in measured and actual volume. It is possible that either imaging time point 1 or 2 depicts the correct volume, or the average of the two. However, one needs to take a closer look at this to see if this is the case. The difference in absorbed dose depending on how volume is measured is substantial at around 10-30% depending on patient and therapy cycle.

Other articles have presented mean absorbed doses to bone lesions at 3.4 ± 1.9 [10], 6.03 ± 8.34 [13] Gy/GBq compared to the 2-point method at 1.84 ± 1.14 Gy/GBq and median absorbed doses 2.97 [13], 3 ± 10 [29] Gy/GBq. For lymph node lesions mean absorbed doses were presented at 2.6 ± 0.4 [10], 15.71 ± 14.72 [13] Gy/GBq compared to the 2-point method at 2.22 ± 1.59 Gy/GBq and median absorbed doses 11.26 [13] and 4 ± 20 [29] Gy/GBq. Such wide range of presented absorbed doses with large standard deviations is not surprising since tumors differ from each other in size and pharmacokinetics. The tumor burden also varies between patients, some having only a few liver lesions while other patients have over 60 bone lesions with no soft tissue lesions. Tumor selection also affects the resulting absorbed doses. Some of the smaller lesions have a large activity concentration resulting in an absorbed doses above the average. The median absorbed dose being lower than the mean is due to these outliers. In this study some tumors had an absorbed dose of over 8 Gy/GBq.

Automated segmentation for tumors is desirable due to the large amount of tumor (some patients having over 60) and how difficult they are to distinguish on CT images. If further investigation on correlation between true volume and volume derived from SPECT images indicate erroneous volumes from SPECT, further methods could be implemented. One possible way is to find a correlation between actual volume (derived from PET, CT or MR images) and the volume from SPECT. It is possible that the SPECT volume differs from actual volume depending on shape and volume (relative difference is larger for smaller more uneven tumor VOIs and smaller for large spherical VOIs). If this is the case a possible solution is to add a factor that represents how the volume from SPECT differ from actual volume into the RC calculations since this value also depends on shape and size.

6.3.4 Comparison of dosimetry methods

There were some difficulties during segmentation and deciding tumor and salivary gland volume. This is a problem for accurately estimating absorbed dose. Comparison of dosimetry methods should not be affected by this in any major way since the methods use the same volume in the calculations. The 2-point method in this rapport uses two imaging time points to estimate a mono-exponential curve, where the initial uptake phase is assumed to be instant. This might be a source of disparity when comparing methods since the 1-point method estimated a tri-exponential curve including an uptake phase. The use of a tri-exponential curve fit used by Jackson et al [3] from three data points is also questionable since more data points should be used for such calculations.

From the Bland Altman plots it appears that the mean difference is not affected by the average absorbed dose. This indicates that the method holds up well for both low and high absorbed doses.

The 24 h imaging time point appears to give results that are more consistent with the 2-point method compared to the 96 h imaging time point, for kidneys, salivary glands and tumors (average volume). Jackson et al [3] presented mean absolute error of population predicted for different organs and imaging time points in their article. According to their results the most accurate imaging time point for salivary glands and kidneys is at around 55 h post injection and 109 h post injection for tumors. It is likely that the 2-point method and 1-point method would present better agreement if imaging had occurred at these times. At 24 h (image 1) they presented that the mean absolute error is lower for kidneys and salivary glands compared to 96 h (image 2) which agrees with results from this rapport. For tumors the mean absolute error at 24 h is 19.5% while at 96 h it is only 5.1%. This is the opposite of the results from this rapport, where the first imaging time point corresponds the best with the 2-point method when using the average volume. The second imaging time point corresponds the best with the 2-point method when using tumor volume from corresponding imaging time point. This is however not a fair comparison since the 2-point method uses tumor volume from both time points when calculating activity.

6.4 Tolerance absorbed doses

Tolerance absorbed doses derived from external beam radiation therapy are 17.5 Gy for kidneys [30], 26 Gy for parotid glands [30] and 39 Gy for submandibular glands [31]. Normal tissues tolerate higher absorbed doses during low dose rates, such as ^{177}Lu-PSMA-617 therapy (compared to external beam radiation therapy) [32], which indicates that the tolerance absorbed doses are higher for these patients. Assuming 6 therapy cycles where the patient is administered 8 GBq per cycle and receives the mean absorbed dose each cycle, the cumulative absorbed dose is 26.9 Gy to kidneys, 14.9 Gy to parotid glands and 17.3 Gy to submandibular glands. This puts kidneys above the tolerated absorbed dose while salivary glands are below the limit with a margin. The difference in cumulative absorbed dose between 1-point method image 1 and 2-point method for kidneys is 0.22 Gy, 0.42 Gy and 1.6 Gy. The disparity between methods should be kept in mind if the 1-point method is implemented for clinical use (under the assumption that the 2-point method is more accurate than the 1-point method). Salivary gland absorbed doses are possibly underestimated due to the previously mentioned limitations during delineation. Before a conclusion for salivary glands is made, absorbed dose calculation should be performed using images were the patient had a head fixation during imaging.

7 Conclusion

During therapy the absorbed dose to kidneys is at risk of exceeding the tolerance absorbed dose, therefore routine dosimetry should be implemented on kidneys. Salivary glands were below the tolerance absorbed dose, other articles have however presented higher absorbed doses than the ones calculated in this study. Therefore it is proposed to do further dosimetry on salivary glands before deciding whether or not dosimetry is necessary for routine clinical use. Dosimetry using the 1-point method is promising. For kidneys and salivary glands the difference in cumulative absorbed dose between methods is small enough that the 1-point method is deemed sufficiently accurate. For patient with known kidney problems, the 2-point method should be used since the 1-point method becomes inaccurate. Dosimetry on images taken 55 h post injection should be evaluated, since this is the most accurate imaging time point to perform dosimetry at, according to Jackson et al [3].
This study was limited by the small sample size. Before any implementations are applied for clinical use dosimetry should be evaluated on more patients.

8 Acknowledgments

I would like to express my greatest gratitude to my main supervisors **Katarina Sjögreen Gleisner**, **Johan Gustafsson** and **Erik Larsson**. Thank you for guiding and supporting me throughout the entirety of this project and making it such a fun and educational process.
I also want to thank **Cecilia Hindorf** for your help at the start of this project and **Anna Sundlöv** for contributing with your much needed medical knowledge.
I would like to thank my classmates for being there with me during my journey of becoming a medical physicist and making it such a fun time filled with great memories. Lastly, I would like to thank my family and friends for supporting me throughout these 5 years.

References

[1] Oliver Sartor, Johann de Bono, Kim N. Chi, Karim Fizazi, Ken Herrmann, Kambiz Rahbar, Scott T. Tagawa, Luke T. Nordquist, Nitin Vaishampayan, Ghassan El-Haddad, Chandler H. Park, Tomasz M. Beer, Alison Armour, Wendy J. Pérez-Contreras, Michelle DeSilvio, Euloge Kpamegan, Germo Gericke, Richard A. Messmann, Michael J. Morris, and Bernd J. Krause. Lutetium-177–psma-617 for metastatic castration-resistant prostate cancer. *New England Journal of Medicine*, 385(12):1091–1103, 2021.

[2] N. Akhtar; O Pail; A Saran; L Tyrell; S Tagawa. Prostate-specific membrane antigen-based therapeutics. *Advances in Urology*, vol. 2012:1–9.

[3] Price A. Jackson; Michael S. Hofman; Rodney J. Hicks; Mark Scalzo; John Violet. Radiation dosimetry in 177lu-psma-617 therapy using a single posttreatment spect/ct scan: A novel methodology to generate time- and tissue-specific dose factors. *J Nucl Med 2020*, 61(7):1030–1036.

[4] O Bergman; L Fredholm; G Hont; E Johansson; P Ljungman; E Wikland; H Nahi; J Zedenius. Cancer i siffror 2018. 2018:52–53.

[5] Ola Bratt. Prostatacancer. 2021-07-02, <https://www.internetmedicin.se/behandlingsoversikter/onkologi/prostatacancer/>.

[6] N Ivanisova. The effectiveness of therapeutic radionuclides (lutetium-177) for prostate cancer treatment in germany. Booking Health GmbH | Diagnosis and treatment(2020).

[7] Nakamura Y et al Hosono M, Ikebuchi H. Manual on the proper use of lutetium-177-labeled somatostatin analogue (lu-177-dota-tate) injectable in radionuclide therapy (2nd ed.). *Ann Nucl Med*, 32(3):217–235, 2018.

[8] F.G. Kondev. *Nuclear Data Sheets*, 159(1), 2019.

[9] AbuQbeitah M. Aygün A. et al Kabasakal, L. Pre-therapeutic dosimetry of normal organs and tissues of 177lu-psma-617 prostate-specific membrane antigen (psma) inhibitor in patients with castration-resistant prostate cancer. *Eur J Nucl Med Mol Imaging*, 42:1976–1983, 2015.

[10] Buxbaum S. Kendler D. et al Scarpa, L. The 68ga/177lu theragnostic concept in psma targeting of castration-resistant prostate cancer: correlation of suvmax values and absorbed dose estimates. *Eur J Nucl Med Mol Imaging*, 44:788–800, 2017.

[11] Allmann J et al Okamoto S, Thieme A. Radiation dosimetry for 177lu-psma i&t in metastatic castration-resistant prostate cancer: Absorbed dose in normal organs and tumor lesions. *J Nucl Med*, 58:445–450, 2017.

[12] Yeyin N et al Kabasakal L, Toklu T. Lu-177-psma-617 prostate-specific membrane antigen inhibitor therapy in patients with castration-resistant prostate cancer: Stability, bio-distribution and dosimetry. *Molecular imaging and radionuclide therapy*, 26:62–68, 2017.

[13] Kamaldeep et al. Examining absorbed doses of indigenously developed 177 lu-psma-617 in metastatic castration-resistant prostate cancer patients at baseline and during course of peptide receptor radioligand therapy. *Cancer biotherapy & radiopharmaceuticals*, 36:292–304, 2021.

[14] Fendler W.P. Kratochwil C. et al Delker, A. Dosimetry for 177lu-dkfz-psma-617: a new radiopharmaceutical for the treatment of metastatic prostate cancer. *Eur J Nucl Med Mol Imaging*, 43:42–51, 2016.

[15] International Commission on Radiation Units and Measurements. Report 85: Fundamental quantities and units for ionizing radiation. *Journal of the ICRU*, 11(1):1–31, 2011.

[16] Wesley E. Bolch; Keith F. Eckerman; George Sgouros and Stephen R. Thomas. Mird pamphlet no. 21: A generalized schema for radiopharmaceutical dosimetry—standardization of nomenclature. Journal of Nuclear Medicine March 2009(50):477–484.

[17] Karen et al Van Audenhaege. Review of spect collimator selection, optimization, and fabrication for clinical and preclinical imaging. *Medical physics*, 42(8):4796–4813, 2015.

[18] Glenn F Knoll. Radiation detection and measurement. *Wiley*, Third edition:231–238, 1979.

[19] Glenn F Knoll. Radiation detection and measurement. *Wiley*, Third edition:265–302, 1979.

[20] Ljungberg Michael and Katarina Sjögreen Gleisner. Hybrid imaging for patient-specific dosimetry in radionuclide therapy. *Diagnostics (Basel, Switzerland)*, vol. 5(3):296–317, 10 Jul. 2015.

[21] E.C. Frey and B.M.W. Tsui. A new method for modeling the spatially-variant, object-dependent scatter response function in spect. *1996 IEEE Nuclear Science Symposium. Conference Record*, 2:1082–1086, 1996.

[22] Kjell Erlandsson; Irene Buvat; P Hendrik Pretorius; Benjamin A Thomas and Brian F Hutton. A review of partial volume correction techniques for emission tomography and their applications in neurology, cardiology and oncology. PHYSICS IN MEDICINE AND BIOLOGY(57):120–121.

[23] Serafeim Loukas. 2020-06-04, <https://towardsdatascience.com/support-vector-machines-svm-clearly-explained-a-python-tutorial-for-classification-problems-29c539f3ad8>.

[24] F. Pedregosa, G. Varoquaux, A. Gramfort, V. Michel, B. Thirion, O. Grisel, M. Blondel, P. Prettenhofer, R. Weiss, V. Dubourg, J. Vanderplas, A. Passos, D. Cournapeau, M. Brucher, M. Perrot, and E. Duchesnay. Scikit-learn: Machine learning in Python. *Journal of Machine Learning Research*, 12:2825–2830, 2011.

[25] K. Sjögreen Gleisner; J. Gustafsson; A. Stenvall; D. Roth; C.Hindorf; L. Jönsson; E. Larsson; T. Olsson; A. Sundlöv. Estimation of tumor burden from 68ga- dotatate-pet/ct and day-7 planar 177lu images, for patients treated with 177lu-dotatate. *Eur J Nucl Med Mol Imaging*, 47:376–377, 2020.

[26] Andersson M; Johansson L; Eckerman K and Mattson S. Idac-dose 2.1, an internal dosimetry program for diagnostic nuclear medicine based on the icrp adult reference voxel phantoms. EJNMMI Research(2017).

[27] Ferdinandus J et al Violet J, Jackson P. Dosimetry of 177lu-psma-617 in metastatic castration-resistant prostate cancer: Correlations between pretherapeutic imaging and whole-body tumor dosimetry with treatment outcomes. *J Nucl Med*, 60(4):517–523, 2019.

[28] ICRP. Report of the task group on reference man. *ICRP Publication*, 23:124–125, 1975.

[29] Richard P et al Baum. 177lu-labeled prostate-specific membrane antigen radioligand therapy of metastatic castration-resistant prostate cancer: Safety and efficacy. *Journal of nuclear medicine : official publication, Society of Nuclear Medicine*, 57(7):1006–1013, 2016.

[30] L Constine M Milano and P. Okunieff. Normal tissue tolerance dose metrics for radiation therapy of major organs. *Seminars in Radiation Oncology*, 17(2):131–140, 2007.

[31] K A. Vineberg J A. Ship C A Murdoch-Kinch, H M. Kim and A Eisbruch. Dose-effect relationships for the submandibular salivary glands and implications for their sparing by intensity modulated radiotherapy. *International Journal of Radiation Oncology*Biology*Physics*, 72(2):373–382, 2008.

[32] R G Dale. Dose-rate effects in targeted radiotherapy. *Phys. Med. Biol*, 41:1871–1883, 1996.

9 Appendix

9.1 Activity uptake

In table 4 the mean activity uptake for the different therapy cycles is presented with corresponding standard deviation. Activity uptake was calculated for the first imaging time point. Activity concentration has been corrected for physical decay to the injection time point. No data for patient 1 soft tissue lesions since this patient had none.

Table 4: Activity uptake of ^{177}Lu-PSMA-617 for organs and tumors. Presented as the mean activity uptake for the different therapy cycles with corresponding standard deviation.

	Patient 1	Patient 2	Patient 3	Patient 4
Activity uptake in kidneys $[ml^{-1}]$	0.012% ± 0.00072%	0.011% ± 0.0016%	0.014% ± 0.0029%	0.015% ± 0.0033%
Activity uptake in submandibular glands $[ml^{-1}]$	0.012% ± 0.0019%	0.0090% ± 0.0034%	0.0039% ± 0.00072%	0.0092% ± 0.0013%
Activity uptake in parotid glands $[ml^{-1}]$	0.011% ± 0.0069%	0.0087% ± 0.0036%	0.0047% ± 0.00090%	0.011% ± 0.00068%
Activity uptake in bone lesions $[ml^{-1}]$	0.018% ± 0.0058%	0.054% ± 0.051%	0.023% ± 0.0057%	0.026% ± 0.017%
Activity uptake in soft tissue lesions $[ml^{-1}]$	NO DATA	0.037% ± 0.024%	0.018% ± 0.0047%	0.023% ± 0.0083%

9.2 Residence time

In table 5 the mean residence time for the different therapy cycles is presented with corresponding standard deviation. No data for patient 1 soft tissue lesions since this patient had none.

Table 5: Residence time of ^{177}Lu-PSMA-617 for organs and tumors. Presented as the mean residence time for the different therapy cycles with corresponding standard deviation.

	Patient 1	Patient 2	Patient 3	Patient 4
Residence time in kidneys [h]	1.20 ± 0.084	1.46 ± 0.040	1.83 ± 0.29	1.67 ± 0.053
Residence time in submandibular glands [h]	0.11 ± 0.021	0.095 ± 0.029	0.043 ± 0.0034	0.077 ± 0.0067
Residence time in parotid glands [h]	0.30 ± 0.0097	0.18 ± 0.060	0.12 ± 0.010	0.17 ± 0.021
Residence time in bone lesions [h]	0.31 ± 0.63	0.43 ± 0.45	0.15 ± 0.14	0.36 ± 0.53
Residence time in soft tissue lesions [h]	NO DATA	0.69 ± 0.50	0.12 ± 0.10	0.35 ± 0.37